DESIGN OF EFFICIENT SOLAR PANELS AND TRACKING/ANTI-TRACKING SYSTEM FOR INTEGRATION WITH THE GRID

A Dissertation Presented

by

Mukhammaddin Zinaddinov

Submitted to the College of Engineering,

University of Massachusetts Lowell,

in partial fulfillment of the requirements for the degree of

DOCTOR OF PHILOSOPHY

2019

Electrical Engineering Program

DESIGN OF EFFICIENT SOLAR PANELS AND TRACKING/ANTI-TRACKING SYSTEM FOR INTEGRATION WITH THE GRID

BY

MUKHAMMADDIN ZINADDINOV

PH.D. CANDIDATE UNIVERSITY OF MASSACHUSETTS LOWELL

SUBMITTED IN PARTIAL SATISFACTION OF THE REQUIREMENTS

FOR THE DEGREE OF DOCTOR OF PHILOSOPHY

ELECTRICAL ENGINEERING

UNIVERSITY OF MASSACHUSETTS LOWELL

Signature of Author: _____

Date: _5/3/19_

Signature of Dissertation Chair: ____Milshtein__ 5|3|19__

Name Typed: _S. Mil'shtein_

Signatures of Other Dissertation Committee Members

Committee Member Signature: ____ Palma __ 5/3/2019__

Name Typed: _John Palma_

Committee Member Signature: _Siavash Pakdelian_ 5/3/2019_

Name Typed: _SIAVASH PAKDELIAN_

Committee Member Signature: _____

Name Typed: _John Bowden_

May 2019

DESIGN OF EFFICIENT SOLAR PANELS AND TRACKING/ANTI-TRACKING SYSTEM FOR INTEGRATION WITH THE GRID

BY

MUKHAMMADDIN ZINADDINOV

ABSTRACT OF A DISSERTATION SUBMITTED TO THE FACULTY OF THE
DEPARTMENT OF ELECTRICAL ENGINEERING
IN PARTIAL FULFILLMENT OF THE REQUIREMENTS

FOR THE DEGREE OF
DOCTOR OF PHILOSOPHY
ELECTRICAL ENGINEERING
UNIVERSITY OF MASSACHUSETTS LOWELL
2019

Dissertation Supervisor: Samson Mil'shtein, Ph.D.
Professor, Department of Electrical and Computer Engineering

This work presents the results of research on potential photovoltaic energy harvesting system improvements on three-levels: semiconductor cell, solar module, and plant-level operation. Several improved-efficiency solar cells that utilize original heterostructure configurations of semiconductor materials with different bandgaps were developed. Results of this research were presented on the IEEE 43rd and 44th Photovoltaic Specialists Conference in 2016-2017 and published in the conference proceedings. Additionally, an original configuration of a light-weight solar panel has been designed and the patenting process has been initiated. The new solar panel configuration is primarily aimed to significantly reduce the weight of solar modules to reduce many associated costs. Theoretical

justifications are provided through calculations and computer models. Prototype tests were constrained by available technology on campus and gave inconclusive results. This work also proposes implementation of a solar threshold-tracking system as a solar power output regulation tool to compensate for instantaneous overproduction of power in the grid. Threshold-tracking (also called anti-tracking) is a calculated curtailment of the solar energy production by means of turning solar panels away from the sun when the energy production exceeds a certain maximum. Threshold-tracking is a new concept and has not been tried before, and it has a potential to grant more flexibility in power regulation and real-time power quality corrections. This work describes threshold-tracking operation mechanisms, feasibility, and outlines possible implementation variations. The abstracts for proposed solar panel configuration as well as anti-tracking were accepted to the IEEE 45th PVSC Conference and will be presented this summer in Chicago. A new mechanical system for solar tracking is also suggested in this work and a prototype assembled. However, limited analysis was performed due to the mechanical nature of the system which puts it out of the scope of this dissertation.

ACKNOWLEDGEMENTS

TABLE OF CONTENTS

LIST OF TABLES

LIST OF ILLUSTRATIONS

CHAPTER I. INTRODUCTION

This dissertation suggests several technological and procedural changes in PhotoVoltaic (PV) technology on a semiconductor cell level, and the solar panel design level to improve the overall efficiency and cost savings of utility-scale photovoltaic systems. The solar PV industry is currently booming, and the historical upward trend of new annual PV installations is likely to continue to grow. In 2017-2018, new global solar installations were 99 GW and 109 GW respectively [1]. Solar and wind will account for 50% of energy production worldwide by 2050 [1]. Government incentives (US & International) such as solar tax investment credits are considered to be the main driver of this growth, indirectly causing ever falling PV module prices. According to Bloomberg NEF, solar panel prices have been consistently following a 28.5% price drop for every doubling of installed capacity since 1976 [1]. Falling prices cause a second-order procurement boost caused by positive feedback between solar panel price drops and PV system installations increase. Such a fast growth of solar energy deployment is fundamentally changing the energy grid, transforming it from centralized and unidirectional to decentralized and bidirectional [2]. Greater need in power production ramping flexibility as well as measures of handling power overproduction were voiced by NREL and 21st Century Power Partnership in 2014 [2], [3]. The International Energy Agency stated that grid flexibility has "unprecedented importance" in power systems due to the rise of PV solar and wind power in 2018 [4]. This dissertation discusses an existing power overgeneration and flexibility problem in the utility-scale solar energy and focuses on solar energy curtailment as a temporary solution

to address these problems. It also points out a deficiency in the currently advocated curtailment methods, proposes an alternative method, and outlines the implementation of the proposed approach. The implementation was not physically tested but only verified to be realizable with current technology.

Chapters II-IV present the results of several new solar cell designs that consist of a-Si/c-Si or CdS/CdSe heterojunctions with p-i-i-n configuration, as well as a cascaded a-Si/c-Si with p-i-n-n-i-p configuration. Some theoretical background and underlying technology will be discussed in this introductory chapter. The following paragraphs describe some basic semiconductor physics principles in photovoltaics, different material technologies and characteristics, and the state-of-the-art in heterostructure solar cell technology.
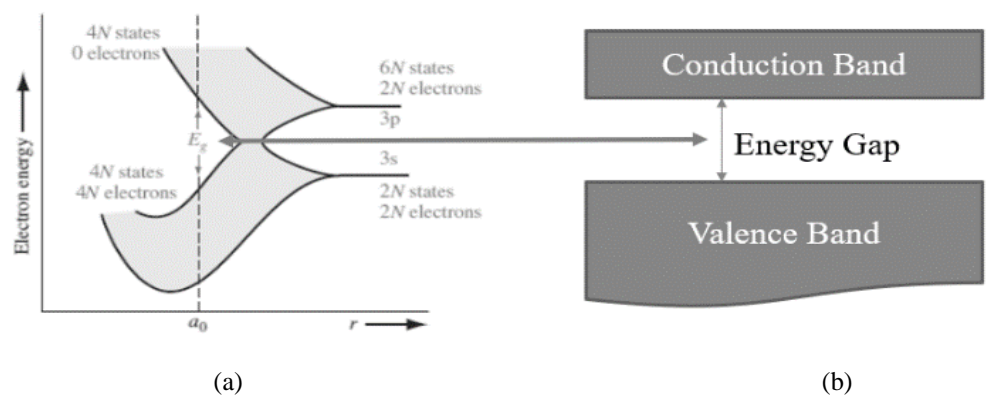
Figure 1 - (a) Energy level distribution in a semiconductor with respect to the distance between individual atoms; Illustration from D. Neaman, "Semiconductor Physics and Devices, 4th ed.", Textbook (b) Typical semiconductor energy diagram.

In an individual atom, electrons can be in distinct energy levels, but as atoms come close to each other, energy levels start interacting. In a semiconductor lattice, electron levels are very close to each other and form energy level clusters and since the distance between them

is negligible, they are assumed to form "energy bands" and can take any energy value within those bands (Refer to Figure 1 (a)). Figure 1 (b) shows a semiconductor energy band in a crystalline lattice (distance between neighboring atoms are equal to the crystal's lattice constant). At an equilibrium, there are no electrons in the conduction band and all electrons are in the valence band. No electrons can occupy energy levels between these bands; this region is thus called a forbidden region or bandgap. Only electrons in the conduction band contribute to current however, thus an excitation of an electron from valence band to conduction band must occur for that electron to contribute to current. The photovoltaic effect occurs when a photon having energy greater than or equal to the energy gap of the semiconductor hits the material, thus exciting an electron into the conduction band and creating an electron-hole pair. It is important, however, to separate an electron-hole pair so it does not recombine right away and thus can contribute to current. In a solar cell, this separation of electrons from holes is done by an in-built potential in the depleted region of the p-n junction. It is then important to note that electron-hole pairs created anywhere other than in the depleted region are going to immediately recombine due to coulombic attraction because there is no other external force that would separate them. This was the motivation to double only the intrinsic layer in our structures described in Chapters II and IV instead of having two monolithically connected standalone heterostructure junctions.

Amorphous, polycrystalline, and monocrystalline silicon materials differ in the number of defects that are present in the crystalline structure. Monocrystalline silicon ideally has no or a very small number of defects because the crystalline structure of a seed crystal is replicated throughout the entire ingot during the Chochralski crystal growth process.

Polycrystalline silicon consists of large grains of multiple uniform silicon crystals. There are multiple crystal dangling bonds and misfit dislocations located across the perimeters of these grains which significantly reduces the lifetime of carriers in a photovoltaic device. This is because Si is a non-direct semiconductor, thus all the recombination processes are non-radiative and adhere to the Shockley-Read-Hall defect recombination method (there are only three methods: SRH, auger, and radiative band-to-band). Auger recombination is very rare because it requires the interaction of three elemental particles and thus is usually assumed to be negligible. Thus, the more defects are present, the higher are the recombination rates, and the lower the average lifetime of carriers. This is shown to decrease the fill factor and the energy conversion efficiency of a solar cell and is highlighted in this 2018 review paper on heterojunction solar cells [5]. Amorphous silicon has even worse defect characteristics because, by definition, this material does not have a crystalline structure. It is extremely cheap, however, and the Silicon technology is mature, which makes the cost of production of solar cells using this material cheaper than competitors.

Multigap solar cells such as tandem and cascaded architectures are more efficient energy transducer because their absorption characteristics are better tuned for solar spectrum [6]. The theoretical conversion efficiency limit for a dual-gap solar cell is 44% and for a solar cell with an infinite number of gaps is 65% [6]. More relevant study from 2014 [7], considered a heterojunction structure where the bottom material is c-Si, and the top is a generalized material with several properties swept within a certain range. This study shows that a material with a bandgap of 1.5 eV like a-Si in tandem with c-Si has a theoretical limit

of 22%, which matches the results of our modelling of cascaded a-Si/c-Si p-i-n-n-i-p cell presented in Chapter III. The highest measured efficiency of a heterojunction solar cell using a-Si/c-Si materials was achieved in 2017 and is 26.7% and the same paper predicts a theoretical maximum output of around 29% [8]. This structure has both anode and cathode contacts at the rear side, in order to improve the optical performance of the top layers. The paper attributes such a high efficiency to contact interface passivation using hydrogen as well as adding a reflective back-surface. Some other heterostructure devices achieved energy conversion efficiencies of over 25% as well [9], [10], and the key denominator of this success seems to be related to contact passivation [5]. Our proposed p-i-i-n structure relies on an advantage of a double intrinsic layer of a solar cell and the simulations show a theoretical efficiency of around 29%. This approach has not been tried before and there is no prior documentation of similar structures. These results are far from the theoretical limit of 44%, however they are based on the structures that use relatively cheap materials with a hope of making it competitive on the market. The three proposed structures were modelled and simulated in SILVACO TCAD software, and the results were presented at the 43rd and 44th Photovoltaics Specialist's Conference and published in the PVSC Proceedings. Each chapter is constituted as a journal publication with proper citations provided. Grammatical errors were fixed, some sentences restructured, figure and table numbers were changed for document consistency, and some clarifications were added denoted with indentations.

In contrast to other solar cell designs, our structures incorporate a double intrinsic layer with a heterojunction located between the two intrinsic layers. This layout is slightly

different from tandem solar cells because those can be considered as monolithically connected independent solar cells (i.e. p-i-n-i-n+, p-i-n-p-i-n compared to the proposed p-i-i-n structures). A cascaded a-Si/c-Si with p-i-n-n-i-p configuration was also designed and published by our group because it required manufacturing steps akin to the ones used for other proposed structures but could produce a relatively higher current density.

Since for an electron-hole pair to be produced, a semiconductor material must be illuminated by a photon with energy equal to or larger than the bandgap, there are certain advantages of having a solar cell made of materials with different bandgaps. The rationale of having a heterostructure double intrinsic layer is to harvest higher-energy photons with a material that has a wider energy gap before those photons would hit a material with smaller band gap and dissipate the excess energy as heat. Heat dissipation is decreased, because on average photons that illuminate the system generate electrons with smaller relaxation energy when excited. If a photon was not energic enough to be absorbed in the first large bandgap layer, it simply continues to propagate to the next layer and will be absorbed there if it has enough energy.

Chapter V presents a new design of a solar panel with a focus on weight reduction and optical and thermal performances comparable to conventional solar panels. A potential 20% weight reduction is demonstrated; this is mainly through the replacement of the front glass cover with hard-coated acrylic. The design was tested for linear stress failure and thermal performance considering internal heat dissipation due to the absorption of light in SolidWorks. The simulations show that the proposed structure performs comparably to

conventional solar panels (marginally better), while having a significantly lighter weight. Weight considerations are important because they affect many auxiliary costs as shipping, handling, installation, as well as recurring costs such as reduced stress on tracking systems.

Chapter VI points out the problem of inevitable solar energy curtailment in the utility-scale solar industry, cost implications of equipment wear introduced by additional heat dissipation and provides a solution for this problem. The ideal solution for this problem would be cheap utility-scale energy storage, however strategies like anti-tracking provided in this chapter could be great for the resolution of the instantaneous energy overproduction problem since it is retrofittable and cheap to implement. The value of this chapter is in drawing attention to the industry trends that naturally lead to the increase in solar curtailment due to relative cost-inefficiency of other approaches, identifying a major problem with the current curtailment methods, and proposing an alternative method which is realizable with the technology currently available on the market. One of the goals of this chapter is to provide enough justifications that anti-tracking as a curtailment method is realizable. This is done by looking at the available technology, their use in similar applications, and outlining the possible structure of an anti-tracking system. Practically, however, such a system was never assembled or tested due to high cost implications of such a project. This is because industrial solar equipment is usually run by Programmable Logic Controllers (PLCs), rugged microcontrollers that are designed for long-term outdoor use. These controllers are current-controlled devices operating in the 4 mA-20 mA range which is an industry standard that makes it compatible with other industrial automation grade parts like Variable Frequency Drives (VFDs) to control AC motors. Replicating an

anti-tracking algorithm using simple microcontrollers like Arduino that controls a relatively small motor would not be a proof of the industrial-scale realizability of the system. One has to demonstrate that there is a technology capable of receiving curtailment signals from the grid, making decision to switch between tracking and anti-tracking, and technology capable of maintaining a set power output threshold by turning solar panels. All these factors as well as a basic system outline were discussed in Chapter VI.

CHAPTER II. DESIGN AND FABRICATION STEPS OF SILICON HETEROSTRUCTURED P-I-I-N SOLAR CELL WITH CORRUGATED SURFACE[1]

Authors: S. Mil'shtein, M. Zinaddinov, N. Tokmoldin, and S. Tokmoldin

Abstract — The current design addresses a few major issues of efficient harvesting of the solar energy. Namely, the ability of the variable energy gap related to the cascaded p-i-i-n a-Si/c-Si structure to absorb a wide energy spectrum avoiding overheating of the device and increasing the number of sun-hours by 30% with no sun-tracking. The novel solar cell consists of a top 0.1 μm thick acceptor doped (10^{16} cm^{-3}) a-Si layer are discussed followed by 2.5 μm of intrinsic a-Si. Next, the intrinsic region is 2.5 μm thick c-Si followed by the 1 μm layer donor doped (10^{16} cm^{-3}) c-Si. The i-i layers, designed with E_{gap1} =1.97 eV and E_{gap2} =1.12 eV, are the most productive generators of photocarriers due to their low rate of recombination. The cascaded design prevents the overheating of c-Si layers, as absorption of high energy photons happens in a-Si layers of the material with E_{gap1}=1.97 eV. In order to improve interaction with the sun as it is low above the horizon (sun rise/sun set), we designed a corrugation of upper layers of our cascaded solar cell. It is very challenging to texture amorphous Si material on the top of the cell. Therefore, we designed sequence of technological steps, where crystalline Si was selectively etched, followed by CVD epitaxy

---

[1] This work was presented on IEEE 43rd Photovoltaic Specialists Conference in 2016 [32]. The manuscript was replicated here with a changed format, as well as figure and table numbers to keep the present document style consistent. The grammatical errors were corrected, and several annotations were added throughout the text for clarification purposes.

of amorphous layers, replicating the surface configuration of c-Si. The designed solar cell has an efficiency of 29.4%, with a filling factor of 0.86. The designed corrugated surface of the cell prolongs the sun hours by about 30%.

I. Introduction

There are several major concepts of p-n junction interaction with the solar spectrum, which define the efficiency of a solar cell; we will list them in sequence of importance from high to low. First, successful harvesting of solar energy could be performed by the devices based on materials which combine various energy gaps: wide E_g at the top of the device and decreasing E_g toward the bottom [11], [12]. This sequence is created in order to prevent the overheating of the solar cell by high-energy photons. It is known that semiconductor solar cells lose 1% of efficiency per every 10˚C of heating up as far as solar energy conversion is concerned[2]. The most important part of the cell design is the intrinsic region of the p-n junction, where recombination of photo-electrons and photo-holes is minimized. Transport and collection of electron-hole pairs is mostly controlled by the Fermi energy profile of the solar cell, so the modeling of energy diagrams should be free from potential barriers preventing flow of electrons and holes to the terminal contacts. In the current study we present the design of an efficient solar cell, where harvesting of solar energy, high rate of generation of electron-hole pairs, and maximum collection efficiency are achieved. Our solar cell is not expected to be installed on a sun tracking system. The prolonged illumination per day of the solar cell is provided by the special corrugation [13] of the

---

[2] Correction: data on solar panels is more abundantly available, they have average temperature coefficients from -0.21 to -0.49%/˚C, meaning that roughly 2-5% of the conversion efficiency will be lost for every 10 ˚C [124], [125].

surface of the device and by using two antireflective layers. We present the design of the heterostructured solar cell made of two materials, namely, a-Si and c-Si, where a diode configuration of p-i-i-n is used. The top intrinsic areas are made of amorphous Si with E_g=1.9 eV followed by an intrinsic crystalline region with E_g= 1.12 eV. Manufacturing steps required for the proposed solar cell production are also discussed.

II. Description of The Solar Cell Structure

The proposed structure consists of a 1 μm thick 10^{16} cm^{-3} n-doped c-Si layer at the bottom, on top of which there are intrinsic c-Si and a-Si regions consecutively (2.5 μm thick each), followed by 0.1 μm thick 10^{16} cm^{-3} p-doped a-Si, 0.07 μm Si$_3$N$_4$ and 0.01 μm SiO$_2$ (see Fig. 2). Application of a very thin acceptor-doped region is needed in order to diminish the photo-generation rate in that region. This allows more photons to pass through to the more efficient intrinsic regions[3] where the electron-hole pairs' recombination rates are low. The intrinsic regions are thicker than the doped layers as that allows creating more electron-hole pairs in the region. Separation of electron-hole pairs and carrier collection are assisted by the internal electric field throughout the depleted region. Ohmic contacts to n-type and p-type regions are provided by 20 Å of the heavily doped (10^{20} cm^{-3}) n$^+$ layer and 20 Å of the 10^{20} cm^{-3} p$^+$ layer. The importance of the a-Si and c-Si cascaded structure is defined by the difference between the energy gaps of these two materials. Having a-Si with an energy gap of 1.97 eV precede c-Si with a 1.12 eV gap on the solar beams' path allows the structure to harvest highly energized photons before allowing them to overheat the c-Si

---

[3] Due to the small thickness of the top layer, very few photons are absorbed in this region, allowing the light to pass to the intrinsic region of the cell. If this region were to be thick, more electron-hole pairs would be generated and, due to the absence of external forces that will prevent their recombination, the solar cell would heat up.

region. This positively affects the life-time of photogenerated electron-hole pairs in the intrinsic crystalline-Si region[4] increasing the overall efficiency of the structure.
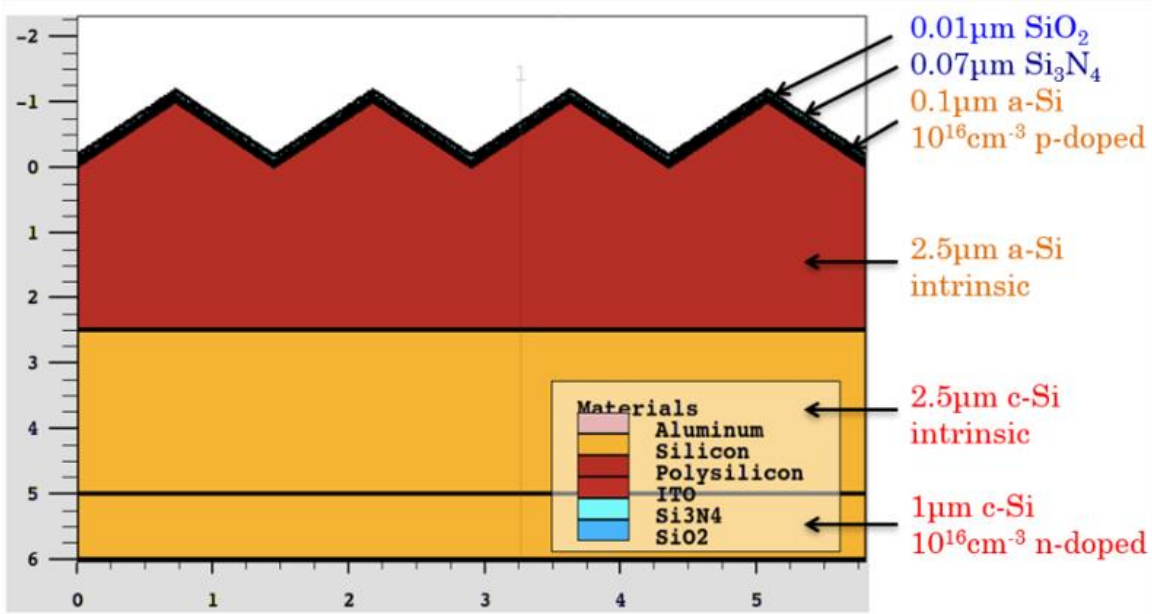
Figure 2 - p-i-i-n solar cell structure fragment[5] (scale is microns by default).

The corrugated surface of the solar cell allows increasing the light trap properties of the structure when the sun is low above the horizon without using high-cost solar tracking systems. Our proposed solar cell structure has corrugated p-doped and amorphous crystalline i-region with 1 μm high and 1.452 μm wide pyramids (in order to achieve the optimal 54° angle [13]). These were covered by 0.07 μm Si_3N_4 and 0.01 μm SiO_2 Double-Layer-Anti-Reflection-Coating (DLARC). The DLARC's thicknesses were optimized [14]

---

[4] Lowering temperature increases carrier lifetime: 1) carrier generation and recombination processes occur all the time but are at equilibrium at a constant intrinsic carrier concentration value specific for a particular semiconductor; 2) when the temperature increases, the carrier thermal generation increases, however an equilibrium must be achieved at some higher intrinsic carrier concentration value; 3) this equilibrium condition necessitates the increase in the recombination rates as well in order to balance the increased carrier generation rate; 4) increased recombination rates are directly related to the shorter carrier lifetime values.

[5] The image is different from the original version but depicts the same structure. The legend shows "polysilicon" as one of the materials, however this is because SILVACO's library does not have a-Si and in order to simulate this material, polysilicon has to be chosen and the defects need to be described manually as shown in some of the examples by SILVACO.

to have overall lower reflection level within 450-1100 nm wavelength range (refer to Fig. 3). Light source specifications in the simulation of the structure were set up so the source emits light in a 400-1100 nm wavelength range. Efficiency calculations were adjusted for the same range.
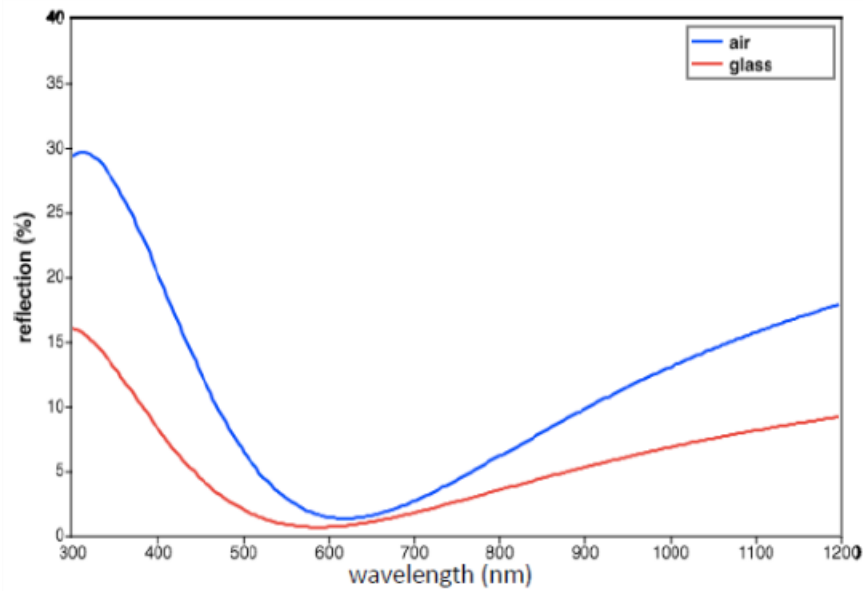
Figure 3 - 0.01 μm SiO2 and 0.07 μm Si3N4 DLARC reflection.

The simulation method applied to this structure was Ray Tracing 2D in SILVACO TCAD. This method takes into consideration reflection and changes in speed/direction of light in the different layers of the structure; it does not, however, account for interferences of the waves in the DLARC region. Therefore, the optimal thicknesses of the DLARC were calculated outside of SILVACO and later used during the device modeling stage.

III. Design and Modeling of the Solar Cell

The simulation of this structure was performed using SILVACO DevEdit and Atlas TCAD (version 5.20.2.R) software, which provide a wide range of tools for process and device

simulations. This section briefly covers some important aspects of the device simulation process. Defining an adequate set of grid nodes of the structure, meshing, is crucial since otherwise it would lead to an incorrect approximation of a device and consequently to in inadequate results. Finite element analysis is the base of SILVACO model simulations, where a high accuracy of grid nodes is required. When the physical structure of the solar cell is defined, the material parameters are introduced into modelling. We started with the refractive coefficients for DLARC and a reflective back contact which are specified by defining the anti-reflection index using interface statements. Then the recombination lifetimes are specified for each of the regions. In our structure, the lifetimes used were 10^{-6} s for p-type a-Si, 10^{-5} s for i-type a-Si, 10^{-3} s for i-type c-Si, and 10^{-3} s for n-type c-Si. The back-reflection parameters were also defined.

IV. Modeling Results

Fig. 4 represents generation/recombination rates of electron-hole pairs throughout the modeled structure. As expected, the generation of photo-carriers is very high in every layer of the device. The recombination rate in intrinsic c-Si is low, however in intrinsic a-Si, the recombination rates are increased due to a large density of electron dangling bonds.
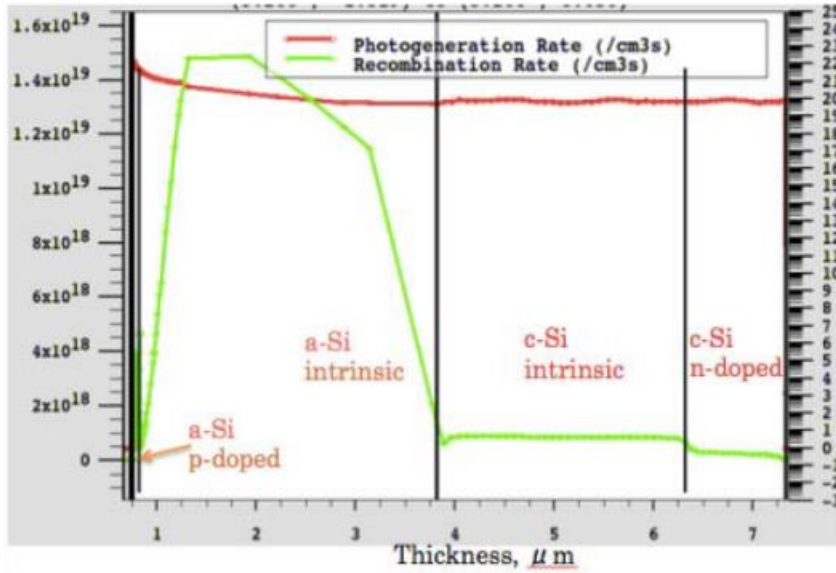
Figure 4 – Photogeneration (right scale) and recombination (left scale) rates.

Fig. 5 shows the energy band diagram of the structure also with the doping. The left side of the diagram corresponds to the top part of the solar cell and the right side to the bottom; dashed vertical lines in the middle represent the interface between amorphous and crystalline silicon regions. Fig. 6 shows the I-V characteristics of the structure.
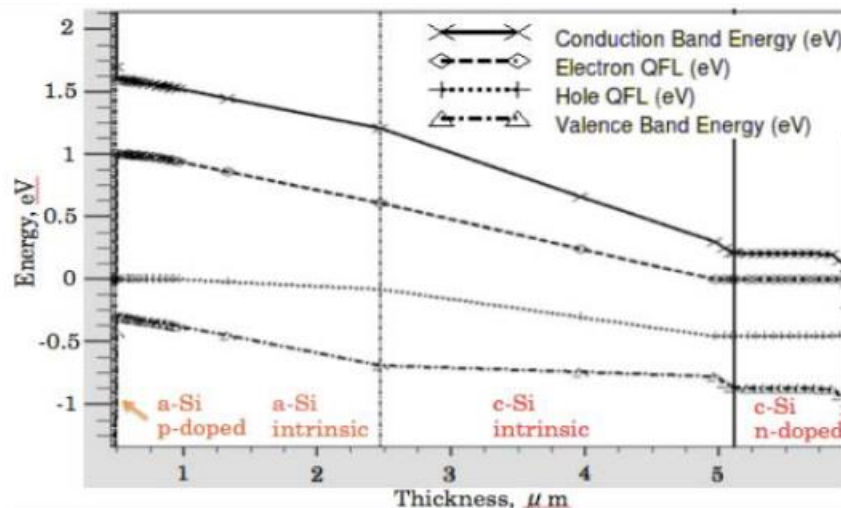
Figure 5 - Energy band diagram of the structure.
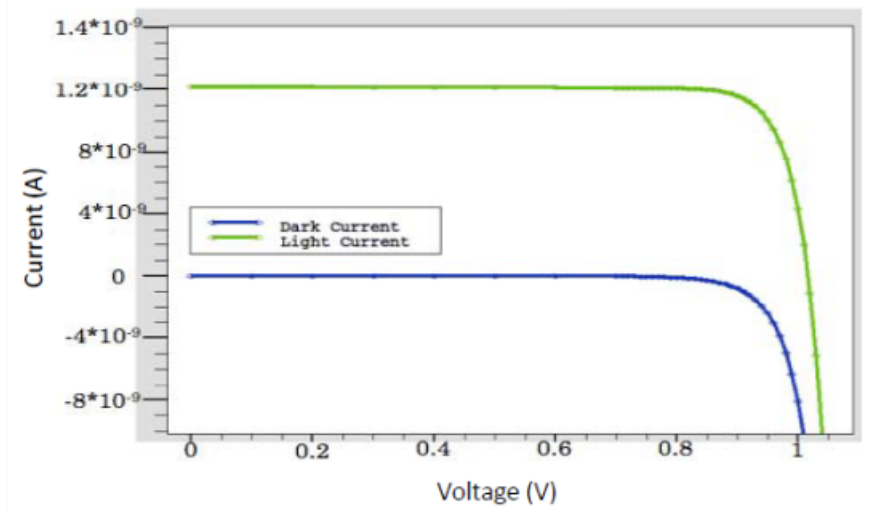
Figure 6 - I-V Characteristics of the Structure.

Table 1 carries solar cell simulation results. The modeling describes a very small cross-section of the solar cell, i.e. 2.904 μm^2.

Table 1 - Major parameters of the structure.

Characteristic	Value
Cross-section area	2.904 μm^2
Jsc	21.4798 mA/cm^2
Voc	1.0843 V
Pmax	$9.52709*10^{-10}$ W
Vmax	0.979995 V
Imax	$9.72157*10^{-10}$ A
FF	0.869906
Efficiency	29.4855%

Annotation: Due to the serial connection of two materials, open circuit voltage of this cell is higher than the usual 0.7V by 50%. The current density is comparable to other c-Si solar cells. The efficiency of 29% is also predicted to be achievable by other a-Si/c-Si cell configurations [8], however is far from a theoretical limit of 44% for a heterostructure cell [6]. Note from Figure 4 that the amorphous silicon has a significantly higher recombination rate than c-Si due to the high presence of defects. This is the main disadvantage of a-Si/c-Si systems, however the relatively cheap price of these materials makes them attractive for the usage in solar cells. Figure 5 shows the differences in bandgaps between the a-Si and c-Si that should help with the thermal energy management. Amorphous silicon has a wider bandgap and thus should absorb higher energy photons while passing the rest to the c-Si layer.

V. Proposed Fabrication Steps

The difficulties to design the processing steps of amorphous layers and prescribe precise plasma parameters and/or annealing temperatures come from the fact that the atomic structure of amorphous Si does not follow the rule of four covalent bonds per atom. Even hydrogenated Si has, at most, 2.7 bonds per atom [15], [16], [17]. Random distribution of the density of dangling bonds in amorphous Si significantly complicates the control of doping, especially donor doping. This is described in many studies and repeated in review [15]. On the macroscale, the presence of voids in this amorphous material undermines uniformity of interfaces of a-Si/c-Si, which is critical for the design of semiconductor junctions. Finally, the degradation phenomena caused by the Staebler-Vronski effect [16] requires certain modifications of fabrication procedures [17]. Although the mentioned

above negative effects are well studied and documented, the attempts of making a-Si/c-Si heterostructure solar cells are motivated by the low cost of materials and production steps and by the maturity of silicon technology.

We would like to suggest the following fabrication steps of our novel cascaded a-Si/c-Si p-i-i-n solar cell: a) Thin layer n-type c-Si produced by Chemical Vapor Deposition (CVD), b) Thin intrinsic layer of c-Si produced by the same technology, c) Corrugation profile created by selective etching of intrinsic c-Si layer. The position of top amorphous layers would replicate the corrugated profile. d) Thin intrinsic and doped layers of a-Si would require Enhanced Plasma Deposition (EPD) of a hydrogenated selection.

VI. Conclusion

The high efficiency of 29.5% was achieved with a novel a-Si/c-Si solar cell design, where cascade i-i layers are built within the same pn junction. This is the major difference from the design of multijunction solar cells. The corrugated surface increases the number of sun-hours by 30%. The random distribution of the density of dangling bonds in amorphous Si impacts the solar cell parameters. This is the reason why commercial companies have their own manufacturing recipes and that is why we suggest only a tentative sequence of fabrication steps: a) The (100) intrinsic layer of the c-Si substrate will be selectively etched to corrugate the surface. b) CVD epitaxy will be used to create the intrinsic c-Si layer. c & d) the intrinsic a-Si/H layer followed by thin p-type a-Si/H layer are deposited by HF plasma. e) The Si3N4 and SiO2 double-layer anti-reflection coating are added as the last steps fabrication steps.

CHAPTER III. CASCADED HETEROSTRUCTURED a-SI/c-SI SOLAR CELL WITH INCREASED CURRENT PRODUCTION[6]

Authors: S. Mil'shtein, M. Zinaddinov

Abstract — In this study, we present a cascaded solar cell with a heterostructure consisting of p-i-n-n-i-p regions. The structure starts with a bottom layer of 0.01 μm thin film p-doped (10^{17} cm^{-3}) c-Si, followed by a 0.44 μm thick intrinsic (c-Si) layer, covered by a 0.1 μm thin n-doped (10^{16} cm^{-3}) c-Si layer. The next stage of the cascaded structure consists of a larger energy gap material which is designed to be 0.1 μm of n-doped (10^{16} cm^{-3}) a-Si, covered by a 0.44 μm thick intrinsic (a-Si) layer and followed at the top by p-doped (10^{17} cm^{-3}) a-Si of 0.01 μm thickness. The described monolithic structure can be considered as a multi-junction solar cell with obvious advantages as compared to existing multijunction solar devices. Most of the thickness of our device is occupied by the intrinsic layers, where high generation of electron-hole pairs is not affected by intensive recombination processes. We avoid the usage of tunneling interconnects, which decrease the total current of the solar cell. The potential step at the energy diagram between the thin layers of n-type of a-Si and n-type of c-Si is negligible, i.e. the collection of carriers from both p-n junctions through the common electrode is efficient. In the conventional stacked multi-junction cells, the total current is equal to the smallest current of a junction in the

---

[6] This work was presented on IEEE 43rd Photovoltaic Specialists Conference in 2016 [24]. The manuscript was replicated here with a changed format, as well as figure and table numbers to keep the present document style consistent. The grammatical errors were corrected, and several annotations were added throughout the text for clarification purposes.

stack. In our design, the two p-i-n structures are combining the currents due to the common terminal created for the a-Si/c-Si n-type interface and due to shorted p-regions. The collected densities of current from amorphous and crystalline cells are 19.87 mA/cm^2 each. The modeled built-in potential, i.e. open circuit voltage, came out to be somewhat smaller than what is currently observed in stacked p-n junctions. In our case, it is about 0.52 V. However, the modeling of this thin-film solar cell demonstrates higher efficiency compared to similar Si heterostructures. The filling factor of designed solar cell is FF= 0.80 and the efficiency is 22.2%. The corrugated top of the solar cell increases the number of sun-hours by 30%.

I. Introduction

The well-established approaches [15], [18] of harvesting the solar energy were demonstrated by the design and fabrication of tandem solar cells, where the top solar cell is made from a wide gap semiconductor serially connected to a cell made out of a smaller energy gap material. The number of cells connected in tandem might vary, but the number of problems related to the alignment of the top and bottom contacts of each cell and unwanted light reflection at the interfaces increases with the number of the cells connected. The bottom junctions of these cells still heat up due to high energy photons and tackling this problem requires specific design solutions. The situation is not better in monolithic multi-junction structures, where the flow of carriers from one junction to another requires the design of tunneling contacts. The challenges of lattice constant matching lead to very costly processing steps. The specific refraction indexes of various layers of the cell cause internal reflections of light. Finally, the total current produced by a traditional sequence of

the p-n junctions turns out to be equal to the current of a smallest photo generator in the chain of junctions. In the current study we propose a heterostructured a-Si/c-Si p-i-n-n-i-p device which is free of the negative effects mentioned above simply because two of our solar cells are in parallel. In contrast to the designs using 300-400 μm Si substrates [12], [19], [20] we suggest the design which should benefit from the thin film technology, where the thickness of common n-type electrodes does not exceed 0.01 μm. The corrugated top of the solar cell increases the number of sun-hours by 30% [13].

II. Modeling and Results

Fig. 7 represents the topology of a three-contact connection configuration. Fig. 8 shows the information about the order of the layers of the p-i-n-n-i-p solar cell, their thicknesses and dopings.
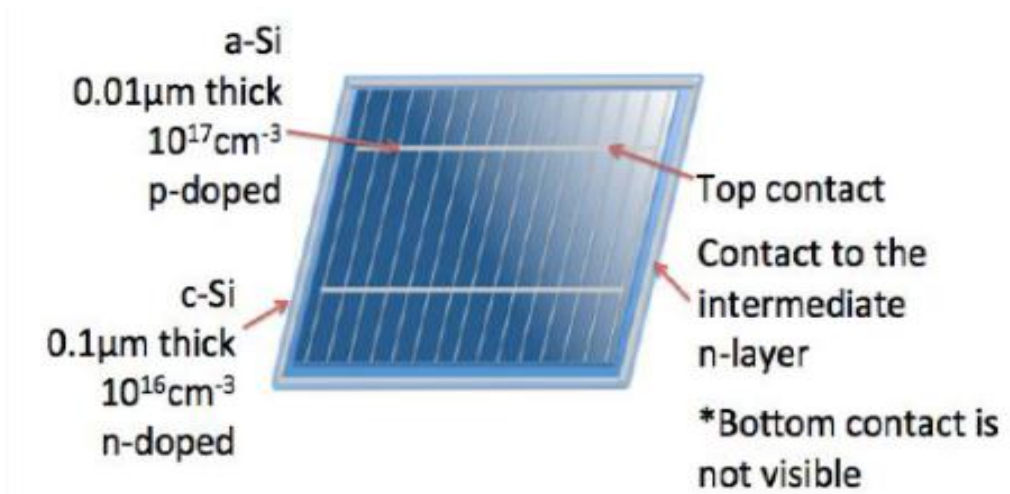
Figure 7 - Layout of the p-i-n-n-i-p contacts configuration.

Annotation: The structure has an intermediate contact grid which can be accessed by etching out the top layer of the a-Si along the perimeter of the cell. This perimeter will then be metallized, to ensure the ease of access to the middle contact during the panel manufacturing stage. Figure 7 attempts to depict the contact layout and access point configurations.
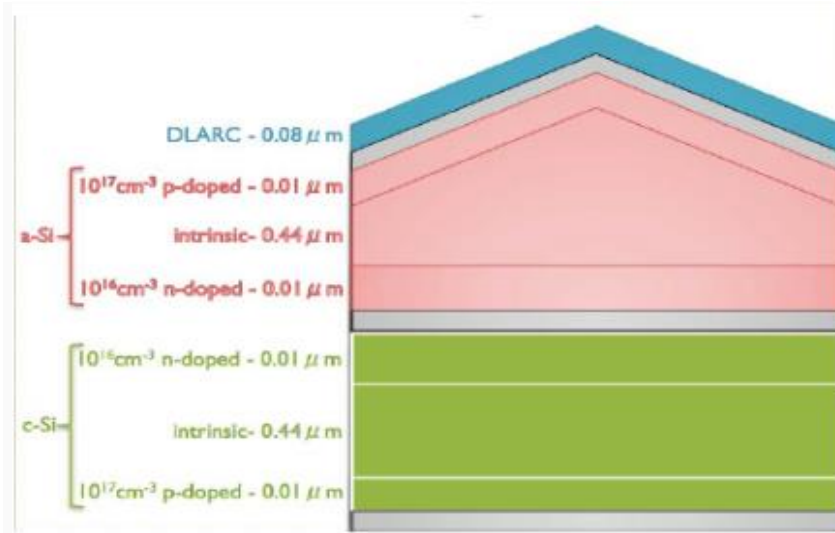
Figure 8 - Sequence of the structure's layers. (Metal contacts are indicated in gray).

Figures 9 and 10 represent the energy bands of the structure and the interface properties of a-Si/c-Si n-layers correspondingly, and Fig. 11 shows I-V characteristics of the modeled device. Table 2 shows a list of the main parameters of the solar cell.
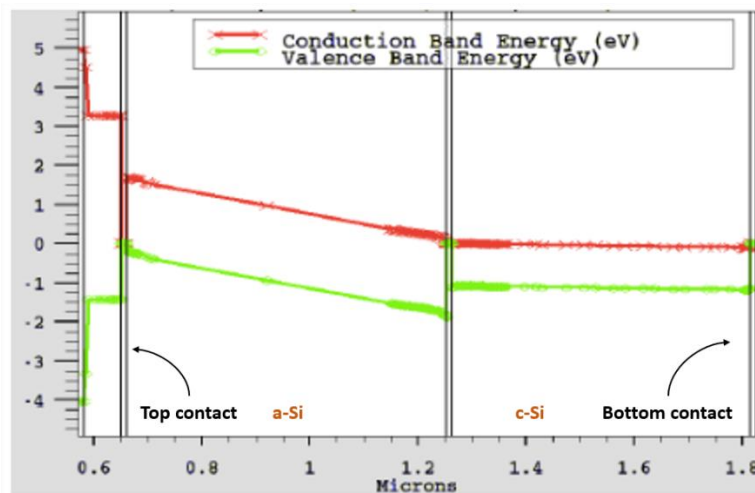
Figure 9 - Energy band diagram of the modeled device.
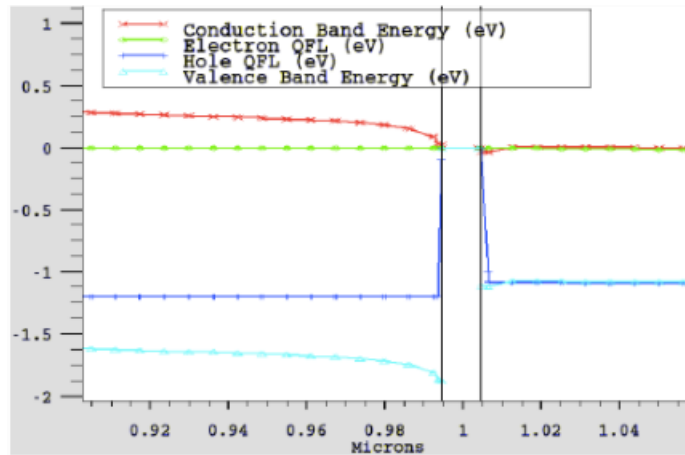
Figure 10 - Energy band diagram of a-Si/c-Si interface.

Annotation: Figure 9 demonstrates the wide-narrow bandgap principle used in this and other solar cell designs aimed to reduce the amount of carrier relaxation energy that converts to heat. Figure 10 is a zoom-in to the interface of the middle contact and the a-Si and c-Si materials. It was ensured that the contact was ohmic in and did not introduce additional resistance to the structure. In real life applications, this would be achieved by overdoping (10^{19} cm^{-3}) 20 Angstrom regions around the contact in both a-Si and c-Si layers.
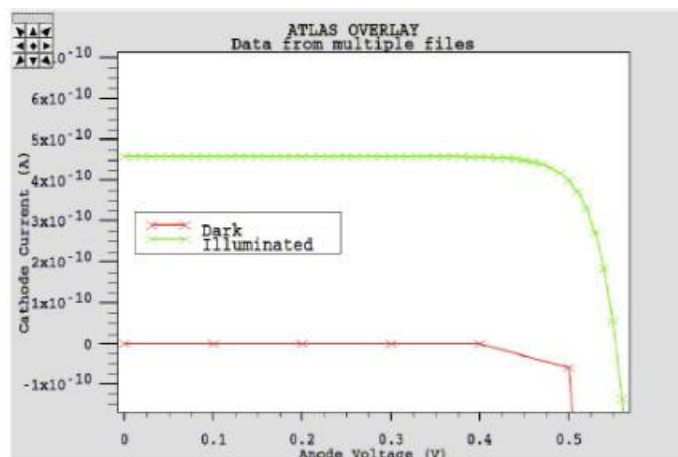
Figure 11 - I-V characteristics of the modeled device.

Table 2 - p-i-n-n-i-p solar cell's main parameters

Parameter	Value
Area	2.904 μm^2
Jsc	40.65 mA/cm^2
Voc	0.52 V
Pmax	$0.48 \cdot 10^{-9}$ W
Vmax	0.44 V
Imax	$1.09 \cdot 10^{-9}$ A
FF	0.81
Effieciency	22%

Annotation: the two tandem structures are connected in parallel and thus double the current through the structure. The open circuit voltage of the whole structure is pulled down to that which is the smallest of the two individual materials. For this reason, there might be some parasitic currents involved that do not contribute to the total current but are circulated between the cells. This is an undesired effect and might negate the thermal management effect achieved by the cascading at the first place. The efficiency value of 22% seems to match the theoretical estimations made by other researchers [7]

III. Conclusions

The described monolithic hetero-structure is a multi-junction solar cell with obvious advantages as compared to existing multi-junction solar devices. Most of the thickness of our device is occupied by two very productive intrinsic a-Si and c-Si layers, where the high generation of electron-hole pairs is not affected by the intensive recombination processes. In a conventional multi-junction solar cell, the total current is equal to the smallest current of the junction in stack due to the serial connection. Two p-i-n junctions in our cell are

similar to what was designed before using a GaAs structure [18] that has common n-layers and a stack that is connected in parallel. In addition, we avoided the usage of tunneling interconnects because they decrease the total current of a solar cell. As thickness of common n-type electrode a-Si/c-Si does not exceed 0.01 μm, it secures an efficient collection of currents from both p-n junctions. Clearly, the designed configuration would be realized best by thin-film technologies. The corrugated top of the solar cell increases the number of sun-hours by 30% [13]. The challenges of a-Si technology are related to the random distribution of density of dangling bonds in the amorphous Si [21], [22], [23]. As a result, the technological steps of a-Si deposition, the uniformity of p-n junctions' interfaces, the degradation of solar cell performance, etc., are treated by commercial companies using their proprietary technologies. The simulation results show: a) The total current density is 40.65 mA/cm^2, Voc= 0.52 V and efficiency 22.3%. b) selected manufacturing steps should provide an etched-down step along the perimeter of the cell until an n-layer (a-Si) stripe 1 mm wide is created at the perimeter of the cell. c) That stripe should be metalized and served as a common contact.

CHAPTER IV. DESIGN OF CASCADED HETEROSTRUCTURED P-I-I-N CDS/CDSE LOW COST SOLAR CELL[7]

Authors: M. Zinaddinov, S. Mil'shtein

Abstract — The dominant presence of silicon in solar cells manufacturing is defined by the maturity of its technology, and low cost of thin film solar cells made from this material. Better efficiency of cascaded solar cells compared to tandem devices was demonstrated in our previous work [24]. It was previously demonstrated that some II-VI compounds are less costly than silicon and very efficient when used in solar cells. We present a novel p-i-i-n cell made of wide-gap, E_g=2.42 eV, CdS and smaller energy gap, E_g=1.74 eV, CdSe. The solar cell consist of a top layer of 0.1 µm thick acceptor-doped (2×10^{18} cm^{-3}) CdS layer followed by 2 µm of intrinsic CdS; next, a CdSe intrinsic region of 2 µm, followed by a 1µm donor-doped (10^{16} cm^{-3}) CdSe bottom layer. The energy diagram of this cascaded solar cell illustrates favorable conditions for the collection of both photo-electrons and photo-holes. The presence of wide-energy-gap CdS at the top of the device significantly minimizes the heat-up effect of the following layers of CdSe. The solar cell demonstrated the following performance characteristics: open-circuit voltage, V_{oc}=1.45 V; short-circuit current density, J_{sc}=23.36 mA/cm^2; filling factor, FF=75%; and efficiency of 18.38%.

---

[7] This work was presented on IEEE 44th Photovoltaic Specialists Conference in 2016 [126]. The manuscript was exactly replicated here with changed format, as well as figure and table numbers to keep the present document style consistent.

Future studies will be focused on the design and production of a CdS/CdSe solar cell deposited on a thin CuO film.

I. Introduction

Successful development of efficient solar cells is built nowadays on the harvesting of a wider range of the solar energy using multiple semiconductor layers with various energy gaps. Thus, most sophisticated solar cells are using either tandem or hetero-structure designs. The success of different semiconductor materials is well reflected in a recent Fraunhofer market study [25]. According to the report, the II-IV semiconductor compounds such as CdS, CdTe and/or CdSe have started to recently prevail in competition with silicon, mostly due to the low cost of thin films of these compound semiconductors. The quantum dots made of CdS and CdSe have already demonstrated 10-17% efficiency [26]. The development of CdTe/CdS solar cells on flexible substrates, with an efficiency of 11%, was reviewed recently [27]. Photovoltaic (PV) solar cells based on cadmium telluride (CdTe) represent the largest segment of the commercial thin-film module production worldwide. Recent improvements have matched the efficiency of multicrystalline silicon while maintaining cost leadership. The United States is the leader in CdTe PV manufacturing, and the NREL [28] has been at the forefront of research and development (R&D) in this area. In Europe, the Fraunhofer research Institute demonstrated in a joint German – French study, the development of tandem SOI solar cells with concentrators having an efficiency of 46% [25]. Efforts to improve the manufacturing technology of CdS and CdSe solar cells continue [29].

The deficiency of Si is defined mostly by a low absorption coefficient [30], which requires the use of thick layers of the material. The relatively small energy gap of Si leads to significant overheating [31] of the solar panels, which in turn decreases the operational efficiency of these widely used panels. Efficiency of silicon-based solar cells was significantly improved by the design of a heterostructure of a-Si/c-Si. Research groups across the world [15], [16], [17] showed that the usage of wide gap amorphous silicon in conjunction with c-Si provides much higher efficiency compared to single-junction polysilicon or single crystal silicon solar cells. Our design of heterostructured thin-film silicon solar cells was different from the other designs, [24], [32]. Offering a heterostructure design with the novel p-i-i-n configuration, we secured the light absorption and generation of photo carriers in two intrinsic regions, where recombination of these carriers is significantly suppressed. The top p-region was designed to be very thin. Similar design ideas are explored in our modeled novel CdS/CdSe p-i-i-n solar cell. Comparing the results of our recent design [33] of a CdS/CdSe 15.6% efficient solar cell with a cascaded p-i-n configuration, we tend to believe that 18.5% efficiency of this paper's heterostructured CdS/CdSe p-i-i-n solar cell is achieved due to thr presence of double intrinsic layers. In this work, we discuss the necessity to insert a buffer layer between the intrinsic regions to match lattice constants of CdS and CdSe. The cost efficiency of novel design is also assessed.

II. Modelling & Design

A. Solar Spectrum Analysis

The structure consists of a CdS and CdSe cascaded cell in a p-i-i-n configuration. A heterostructure solar cell with two intrinsic regions of different band gaps allows harvesting of photons more efficiently. Photons with shorter wavelengths are collected in the first CdS i-region with a wide bandgap (Eg=2.42 eV), and the remaining electrons are collected in the next intrinsic region of CdSe (Eg= 1.74 eV). This improves the thermal characteristics of the cell because high-energy photons do not heat up the following layers of semiconductor with smaller energy gaps. Figure 12 shows the energy band diagram of the novel cell. Our calculations showed that 30% of the light within a spectrum of 0.4 - 0.71 µm. is collected by the first region and 70% by the bottom. The simulations also showed that the number of generated electron hole pairs was in the order of 10^{17} $s^{-1} \times cm^{-2}$ which corresponds to the number of photons in the given range.
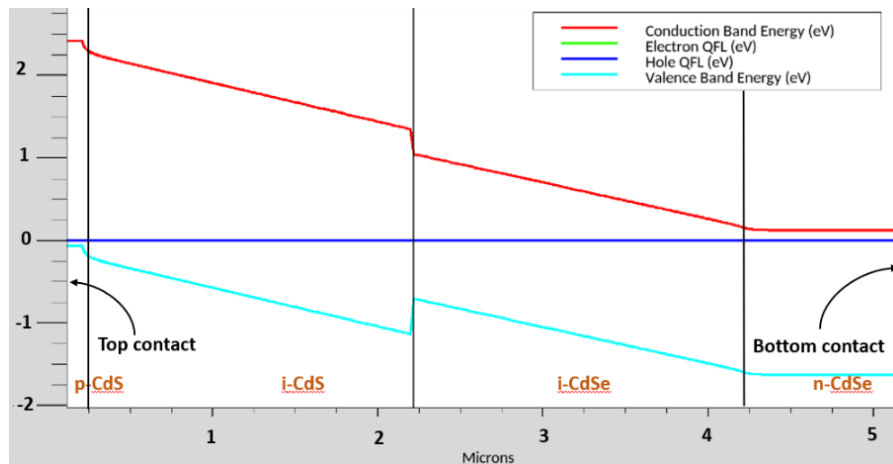
Figure 12 - Energy bands diagram of the CdS/CdSe cascaded p-i-i-n solar cell.

B. Layer Thicknesses and Doping

Design choices of the region thicknesses are described in this section. The optimal configuration was expected to have a relatively smaller p-region and large i-regions. This is due to the fact that all electron-hole pairs created in that region will immediately recombine, unlike inside of a p-i-i-n junction where carriers will be pulled apart by the build-in field. To maximize the light absorption, it is advantageous to have intrinsic regions relatively thick. If they are too thick, however, the strength of the build-in field decreases, in turn decreasing efficient harvesting of solar energy. Layer thickness sweep simulation showed that the optimal thicknesses for the regions are 0.1 µm for p-doped CdS, and 2 µm for both intrinsic CdS and CdSe. Our calculations with the extremely small lifetime of carriers in CdSe [34] motivated us to use the thickness of 0.1 µm for n-doped CdSe to decrease electron-hole recombination in that region and make the n- region smaller than the diffusion length, while keeping it thick enough for potential CVD manufacturing processes.

Design choices regarding the doping configuration where governed mainly by a need to have the built-in potential across the junction as large as possible, while keeping the recombination of majority and minority carriers in p and n regions as small as possible to achieve maximum efficiency. Our modeling showed that having 2.3×10^{18} cm^{-3} of acceptors in the p-doped CdS region with 10^{16} cm^{-3} donors in the n-doped CdSe region provides optimal solar cell efficiency. In this simplified model, it was assumed that the regions are doped uniformly.

III. Modeling Results

Figure 13 shows the I-V curve of the designed cell. Characteristics of the simulated solar cell are shown in Table 3.
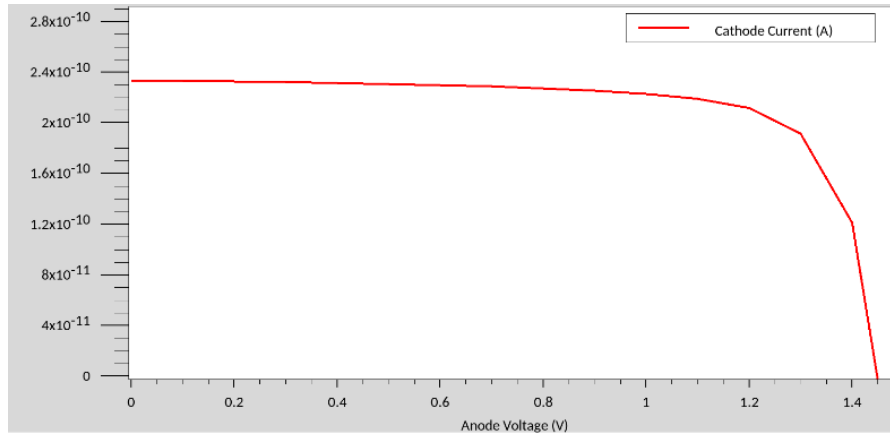
Figure 13 - IV relationship of the CdS/CdSe cascaded p-i-i-n solar cell.

Notice that the modeled cross-section of the device was set to be 1 μm^2, so the current values that are shown on the graph should be converted into current densities to be compared to other solar cells.

Table 3 - CdS/CdSe solar cell characteristics

Jsc	23.36 mA×cm^{-2}
Voc	1.449 V
Pm	25.37 mW×cm^{-2}
Vm	1.200 V
Im	21.15 mA×cm^{-2}
FF	74.99%
Eff	18.38%

Annotation: small fill factor (FF) significantly affects the efficiency of the cell. One can note that the voltage at the maximum power point is 30% less that the open-circuit voltage

of the entire cell and this seems to be causing a sudden drop in FF. The theoretical efficiency of this cell, however, is comparable to the measured performance of silicon cells. It should be noted, however, that measurements of a CdS/CdSe manufactured cell are required to make any reasonable comparisons.

IV. Economic Evaluation

The prices for raw materials being compared demonstrate that Si is about twice as expensive than CdS and one and a half times more expensive than CdSe [35], [36], [37]. Thin-film processing, however, depends on technology steps used, i.e. sputtering of Si is still less expensive than sputtering of CdS [38], [39]. In the production of single crystals using epitaxial technology, Si appears to be more expensive [40], [41].

V. Conclusions

The novel heterostructured CdS/CdSe p-i-i-n solar cell was designed to demonstrates the efficiency equal 18.4% with V_{oc}=1.45 V and short-circuit current density J_{sc}=23.36 mA/cm^2, which is better than solar cell from the same materials designed by our group in 2012 [33]. The low cost of thin films [40], [41] of CdS and CdSe compared to Si is a major factor moving technology of II-IV compound semiconductors to the forefront of solar cells market. We are planning to select epitaxial technology for production of these solar cells in the nearest future. Depending on the selected technology, we will design a buffer layer of graded CdS – CdSe, which should not exceed 30-40 Angstroms in thickness.

CHAPTER V. LIGHT-WEIGHT SOLAR PANEL STRUCTURE[8]

I. Problem Statement:

PV solar energy's initial investment is affected by shipping, handling, and operating costs. These are directly related to solar panel's weight, frame structure strength, and speed of installation. This motivates designing a new solar panel structure that has optical, thermal, and lifetime longevity performance comparable to traditional panels while significantly reducing its weight. Additionally, the new panel structure must be compatible with the existing mounting solutions on the market in order to be competitive.

II. Introduction

This chapter proposes a new solar module design with reduced weight but with thermal and optical performance no worse than the traditional solar module structure. The reduction of weight was achieved by replacing the top glass layer with acrylic and changing the structure of the frame to provide better stress resilience. The proposed structure is shown in Figure 14 and it addresses industry defined objectives and constraints stated in the following sections. Optical, thermal, and structural aspects of the design were calculated and modeled. Design choices and justifications are also discussed. Such important issues as retrofittable connection holes, speed of installation, and manufacturability were acknowledged, however not addressed in detail due to available testing equipment

---

[8] This work was done with the help of the students from the Plastics Engineering Department at UML, S. de Cleir and T. Zannoni, under Dr. D. Kazmer's supervision.

limitations. Nonetheless, the proposed structure calculations and modelling indicate a potential for improving a solar module product.
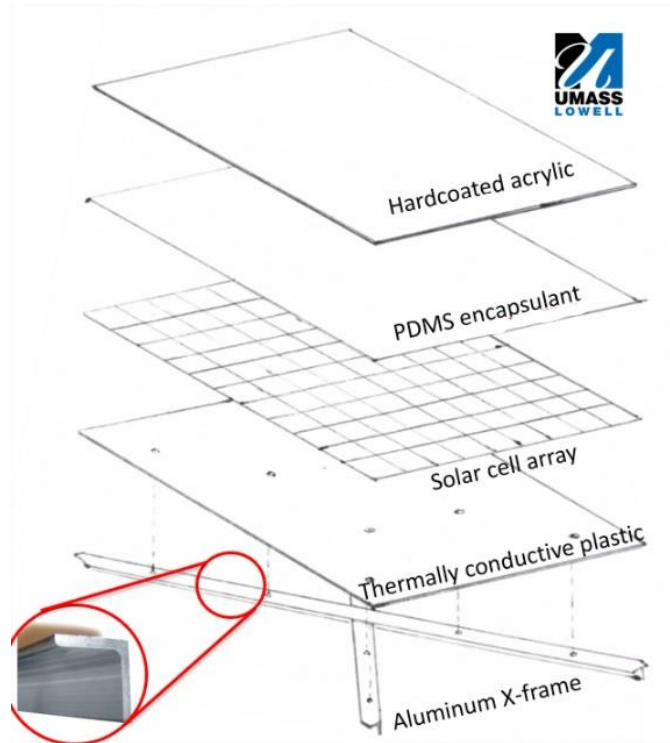
Figure 14 - Proposed light-weight solar panel structure.

III. Objectives & Constraints

A. Weight Considerations

Solar panel weight reduction affects the shipping and handling costs. Large items are often charged for shipping based on volume and total mass because shipping trucks and containers have a certain weight capacity limitation and associated fuel cost expenses. The weight of solar panels also affects the number of worker-hours required for its installation. According to NREL cost benchmark [42], shipping and handling costs accounted for 9-12% of a PV module's cost in residential PV installation. In utility-scale installation, these

costs are less transparent (lumped together with planning, logistics, and warehousing) and account for a fraction of 8-13% [42].

For residential and non-residential rooftop installations, US EPA requires installers to submit code-compliant documentation that a rooftop that can support additional 6 lbs/sq.ft of dead weight [43]. For utility-scale solar, the high weight of modules necessitates having deeper piers for solar mounting, which also increases the total weight placed on land and increase settlement (this concern was brought up in a study regarding solar stations on landfills [44], but it translates well on regular power plants as well).

A solar panel's weight reduction while keeping the same volume and performance parameters might decrease the total costs of PV installations and make certain marginal projects more cost-effective. Decreased weight and reinforced structure (good handling of stepping and withstanding microcracks) were two of the biggest requests when talking to PV installers by our research group.

B. Optical Considerations and Soiling

When a new solar module structure is proposed, material thicknesses and their refraction coefficients need to be carefully selected for the optimal optical performance. When light passes through one media to another, we consider three components: reflected light, absorbed light, and transmitted light. The amount of reflection and transmission at a normal

incidence depend on the refraction indices of two materials and can be calculated using Fresnel's Equations (5.1-5.2):

$$R(f) = \frac{(n_1(f) - n_2(f))^2}{(n_1(f) + n_2(f))^2} \qquad (5.1)$$

$$T(f) = \frac{4n_1(f)n_2(f)}{(n_1(f) + n_2(f))^2} \qquad (5.2)$$

where R is the reflectance, T is transmittance, n_1 and n_2 are refraction coefficient of the materials for a specific frequency of light, f. If $I_o(f)$ is the intensity of incident light of a given frequency,

$$I_{in}(f) = I_o(f) * (1 - R(f)) \qquad (5.3)$$

is the amount of light that entered the second media. The Beer-Lampard Law is then used to calculate the amount of light absorption in the material:

$$I_{out}(f) = I_{in}(f) \times e^{-\alpha(f)x} , \qquad (5.4)$$

where $I_{out}(f)$ is light intensity leaving the second media, α is the absorption coefficient for a given frequency, and x is the thickness of the media. Equations 5.1-5.4 will be used when estimating optical and thermal performances (light absorption affects material temperature).

Another factor indirectly affecting the optical performance of the module design is power loss due to soiling. According to NREL's paper from 2005 [45], losses due to soiling are around 5%, but can account for anywhere between 2-25%. A much more recent study observed 186 Californian PV stations all year in 2010 and the data showed that soiling

losses can be modeled linearly at 0.05% efficiency loss per day (around 7% loss in 145 days) [46]. Considering that module cleaning and vegetation management is the second largest expense in utility-scale PV, the issue of soiling needs to be kept in mind in the new solar module packaging design process.

C. Reliability and Lifetime Considerations

Wind load standards are still emerging, but many solar systems deployed are designed to withstand 120 mph wind gusts; installations for wind speeds up to 175 mph are reported [47]. Golf ball impact with the module was planned to be simulated, however the impact force of this interaction strongly depends on the contact time duration and no reliable data was found regarding that. The solar module was CAD tested for stress when being stepped upon since this is one of the big concerns during the installation process. The installer company that we talked to complained that their workers step on the panels all the time and they recently introduced a monetary penalty per step. The average weight of an American man is around 90 kg and will be used in simulation tests of the new panel along with an approximate foot area of size 9. Additionally, materials resistant to degradation due to prolonged UV and water vapor exposure have to be selected.

D. Manufacturing and Retrofitting Considerations

This work will propose an X-frame structure, but the discussion about retrofitting and compatibility with the existing mounting structures will not be discussed. This is because frameless solar panels are present in the market, as well as an abundance of solutions of

how to mount them both on the roofs and tracking systems. Minimal changes can be introduced to the design to target one or another mounting system. Manufacturing considerations will be briefly addressed, and a preliminary assembly process will be described, to estimate the feasibility of a scalable module production.

IV. Design Choices & Justifications

Modern day solar panels traditionally consist of five layers of materials (refer to Figure 15). Initially, Ethylene Vinyl Acetate (EVA), which is laid between the glass and semiconductor material, covers the solar cell's grid [48], [49]. Then the back of solar cell is covered with another layer of EVA and a protective PolyVinyl Fluoride (PVF), called "tedlar", back-sheet. The entire sandwich is heated in the oven for the EVA to crosslink and for the Tedlar layer to adhere. The entire structure is then covered by glass and framed in aluminum. This solar panel structure, and special materials like EVA and PVF used to hermetically seal the structure, are commonly used in nowadays solar panel production [50], [51], [52].
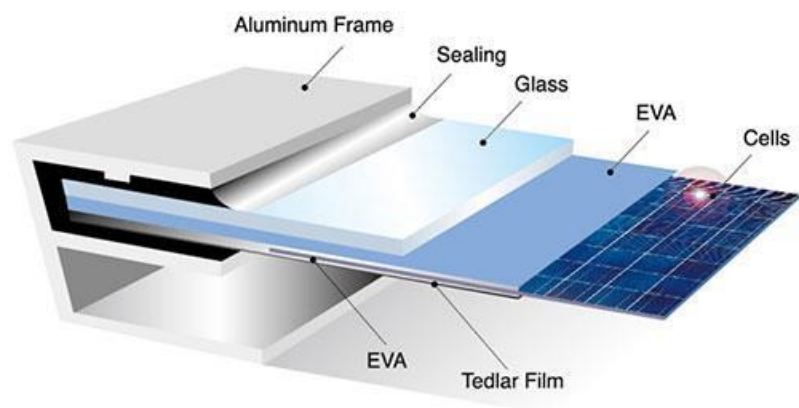
Figure 15 - Conventional solar panel structure [53]

Contrary to existing technology, the tempered glass that is traditionally used in solar modules was replaced with a UF-3 acrylic in our design in order to significantly reduce structural weight. Acrylic's mass density is more than two times smaller than that of glass and it is also less brittle due to higher elasticity. This specific grade of acrylic was chosen in order to prevent almost all light shorter than 410 nm from illuminating the PV cells. Since Silicon technology is dominating the PV market, the new packaging should be focused on transmitting the light spectrum that is suited for the absorption by this material. The Si bandgap is 1.12 eV which corresponds to the absorption of photons with wavelengths shorter or equal to 1107 nm. The higher the photon energy, however, the more excess energy it is going to dissipate upon absorption. With increasing heat, the efficiency of Si solar cells decreases. UF-3 acrylic is abundantly used on the market specifically for the purpose of blocking UltraViolet (UV) light. Table 4 shows some of the aspects that influenced using acrylic instead of glass in a new solar module structure. Light transmission coefficients of glass and acrylic over a wide range of wavelengths is provided in Figures 16 and 17 (note that only wavelengths up to 1107 nm need to be considered in a Si solar module design).

Table 4 - Acrylic and glass comparison

Property	Acrylic	Glass
Density (g/cm^3)	1.18	2.7
Light transmission	~92%	~90%
Cost ($/sq.ft, 1/16 in.)	$2 [54]	$5 [55]
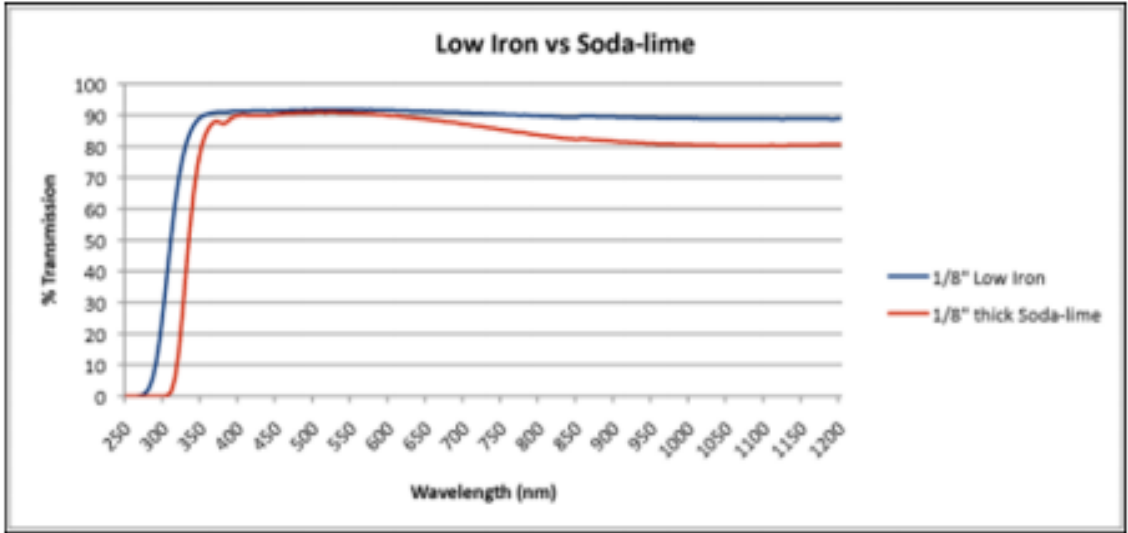
Figure 16 - Light transmission coefficient of common glass materials [56].
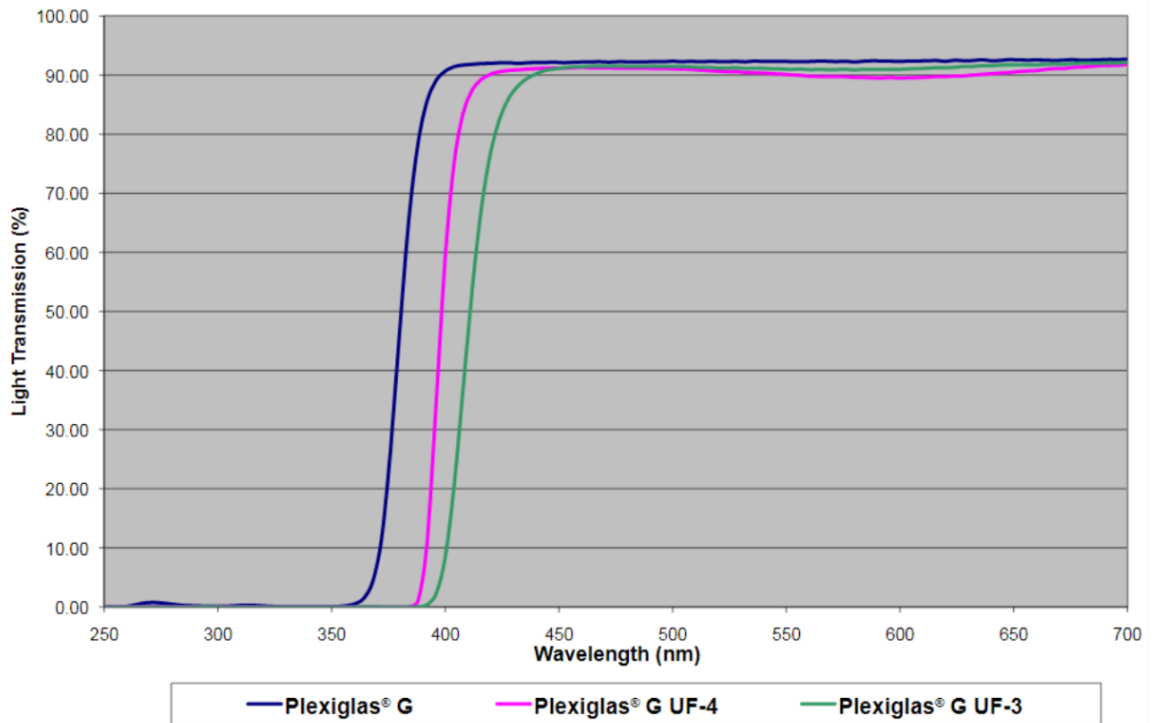
Figure 17 - Light transmission coefficient of several acrylic variations available on the market [57].

Three-millimeter-thick Thermally Conductive Plastic (TCP) based on a PA6 polymer (Celanese COOLPOLY® D3612) was selected as a module back sheet instead of a conventional PVF film. This was done in order to be able to mount an aluminum X-frame at the back for structural support. The use of the X-frame that consists of standard 0.125" thick aluminum L-bars was chosen instead of a traditional picture-frame configuration because it significantly reduces bowing under locally applied loads, or high winds. Structural stress simulations in SolidWorks under different loads are provided in later sections. TCP's thermal conductivity is 1.3 W/m-K which is ten times better than PVF's 0.13 W/m-K. TCP is however 3 mm thick and PVF is a film of only two to three tenths of a millimeter-thick.

In the new design, PolyDiMethylSiloxane (PDMS) is used as an encapsulant instead of EVA because it does not require the use of elevated temperatures for crosslinking and thus can be safely used in conjunction with other plastic materials. PDMS is also already widely used in the solar industry as an encapsulant. It is a mature and familiar technology and this factor usually has positive monetary implications in terms of mass manufacturing.

Tables 5 and 6 contain comparative information about both the conventional and new solar module structures. Glass thickness was measured from solar panels available in our lab, various film thicknesses were estimated based on datasheets of similar products (they are all fractions of a millimeter). Three-millimeter-thick acrylic and TCP layers were used in calculations because this is a standard thickness for an extruded plastic and might be beneficial in terms of cost due to economy of scale. Weights of aluminum frames for both

modules are assumed to be approximately the same and around 2.5 kg. These estimates show that a new panel structure with 20% reduced weight is achievable.

Table 5 - Traditional solar panel structure.

	H (mm)	L (mm)	W (mm)	Vol. (m^3)	Density (kg/m^3)	Mass (kg)
Glass	4.5	1500	750	0.0050625	2500	12.65625
EVA	0.1	1500	750	0.0001125	960	0.108
Si	0.2	1500	750	0.000225	2330	0.52425
EVA	0.1	1500	750	0.0001125	960	0.108
PVF	0.3	1500	750	0.0003375	1500	0.50625
TOTAL MASS: 13.90275 kg (+2.5kg aluminum frame)						

Table 6 - Proposed solar panel structure.

Table 2. Proposed solar panel structure	H (mm)	L (mm)	W (mm)	Vol (m^3)	Density (kg/m^3)	Mass (kg)
Acrylic	3	1500	750	0.003375	1180	3.9825
PDMS	0.5	1500	750	0.0005625	965	0.5428125
Si	0.2	1500	750	0.000225	2330	0.52425
EVOH	0.1	1500	750	0.0001125	960	0.108
Therm. Cond. Plastic	3	1500	750	0.003375	1600	5.4
TOTAL: 10.557563 kg (+2.5kg aluminum frame)						

Readily available materials were favored in the design. This is expected to significantly reduce the self-cost of solar panels due to low material and component cost. The simplest manufacturing techniques were preferred in order to reduce the fabrication costs and many manufacturing steps have a potential to be automated. Mounting holes location can be easily adjusted for the new module design to be compatible with the existing mounting frames on the market. Suggested manufacturing steps are as follows, however there is a lot of potential for optimization:

1. X-frame assembly from two aluminum L-bars (0.125'' thick).

2. Drilling attachment holes in aluminum frame.

3. Drilling holes in TCP back sheet.

4. Attaching TCP to the X-frame with screws, nuts, and locking washers.

5. Filling the TCP holes with silicone RTV and levelling the surface.

6. PDMS application (1/2).

7. Laying out the solar cell arrays.

8. PDMS application (2/2).

9. Covering the surface with an acrylic sheet right after PDMS application.

10. PDMS curing.

11. Framing the panel with U-channel plastic bow filled with Silicone RTV sealant.

V. Alternative Solar Panel Designs

The conventional solar panel design described in Section IV is the predominant solar panel configuration on the market today. It can be implemented using both monocrystalline or polycrystalline solar cells. Three main alternative solar panel structures are thin-film solar panels, a double-glass solar panel structure, and frameless solar panels. Thin-film solar panels are built by depositing the semiconductor materials directly onto a glass or plastic (sometimes flexible plastic) bases through chemical vapor deposition or similar techniques (without using semiconductor substrates) which is then encapsulated with a back-sheet.

This manufacturing technique is ideal for mass-production, however it limits the semiconductor material used to only the amorphous options (crystalline structures cannot be deposited additively). Amorphous structures on their own inherently have many defects and thus very small efficiencies of around 10-11% [58], [59], [60]. Such small efficiencies make them highly cost-inefficient in many residential and utility projects. Double-glass solar panel structures, however, are similar to the conventional solar panels, but they use bifacial solar cells as well as a glass back-sheet instead of a Tedlar film. The main application for these solar panels is the ability to harvest direct and reflected solar light [61]. However, glass is a poor thermal conductor and sandwiching the photovoltaic cells encapsulated in EVA between two glass sheets might limit their application market to only some northern, colder states. Finally, the frameless solar panel design is primarily motivated by aesthetic reasons, however it suffers from the lack of a variety of mounting options that are available on the market [61]. The solar panel design proposed in this chapter however, provides an option of connecting to the X-frame to which any additional buffer interface can be designed with simple manufacturing steps and attached if needed.

VI. SolidWorks Structural Modelling Results

A. Simulation Assumptions and Failure Criterion

Material properties from different sources [57], [62], [63], [64], [65], [66], [67] used for this and other simulations are provided in Table 7. Properties that are used to conclude whether the solar module passed the simulation tests are highlighted in green. Yield strength is the minimum stress value after which the material deforms plastically; compressive strength is the maximum compression stress value that a material can

withstand without breaking. Factor of Safety is a parameter used to indicate how much stronger the material is with respect to the applied load and is equal to the ratio of yield strength to working stress. For example, a safety factor of 10 for a load of 1000 N means that the part material can handle 10 times more load. SolidWorks allows us to plot safety factor parameters with respect to yield strength values and this feature was used in the current study. The software recommends using the Max von Misses stress criterion for ductile materials and the Mohr-Coulomb stress criterion for brittle materials. The difference is that the Mohr-Coulomb criterion also considers compressive strength of the material while Max von Misses does not. Since silicon region of a solar module is very thin with large area, it is computationally consuming to mesh it in SolidWorks (although ANSYS provides much more flexible mesh refinement tools). For this reason, Si was not specifically included in the model, and the factor of safety for Si is applied for the two bordering regions, TCP and PDMS. The reason for this is that if the safety factor tuned for Si fails in these two regions, it will also fail for Si due to its close proximity.

Table 7 - Simulation material properties

Name:	UF-3	PDMS	Silicon	TCP
Model type:	Linear Elastic Isotropic	Linear Elastic Isotropic	NA	Linear Elastic Isotropic
Default failure criterion:	Max von Mises Stress	Max von Mises Stress	Mohr-Coulomb Stress	Max von Mises Stress
Yield strength:	7.2×10^7 N/m^2	0.7×10^6 N/m^2	1.2×10^8 N/m^2	3.75×10^7 N/m^2
Tensile strength:	7.2×10^7 N/m^2	2.24×10^6 N/m^2	1.2×10^8 N/m^2	6.65×10^7 N/m^2
Compressive strength:	1.05×10^8 N/m^2	1.65×10^8 N/m^2	3.3×10^9 N/m^2	6.8×10^7 N/m^2
Elastic modulus:	3.1×10^9 N/m^2	1.7×10^6 N/m^2	1.1×10^{11} N/m^2	2.4×10^9 N/m^2
Poisson's ratio:	0.35	0.46	0.28	0.35
Mass density:	1190 kg/m^3	970 kg/m^3	2300 kg/m^3	1620 kg/m^3
Thermal expansion coefficient:	7.02×10^{-5} /Kelvin	7.02×10^{-5} /Kelvin	7.5×10^{-6} /Kelvin	10.1×10^{-5} /Kelvin

B. Wind Load of 120 mph

Wind load was calculated using Equation 5.5:

$$F_w = \frac{1}{2} * \rho * v^2 * A ,\qquad(5.5)$$

where F_w is wind force, ρ is air density (taken as 1.2 kg/m³ in this case), v is wind speed, and A is the area of the panel. Using this equation, one can get a wind load value of 1968 N for a 120 mph wind gust. This load was applied normally to and evenly distributed across the entire face area of the panel. Stress values throughout the Si region were well below the yield strength value. The cross section shows that the silicon region experiences less than 10 GPa of stress while the yield strength of Si is 120 GPa. Note that max stress occurs at the fixture contacts and not the Si module region (refer to Fig. 18-19). Figure 18 shows the cross section view of the panel to demonstrate that no internal stress peaks occur inside of the panel. The maximum deflection observed was 12 mm and is shown in Figure 20. Study results are provided in Table 8; safety factor values for every material are well above unity, meaning the proposed design should be able to handle wind loads of 120 mph.

Table 8 - Wind load study results

Name	Type	Min	Max
Stress	VON: von Mises Stress	582.7 N/m^2	8.439×10⁸ N/m^2
Displacement	URES: Resultant Displacement	0 mm	12 mm
Acrylic Safety Factor	VON: von Mises Stress	25.46 N/m^2	2.631×10³ N/m^2
PDMS Safety Factor	VON: von Mises Stress	10.84 N/m^2	1.694×10³ N/m^2
Silicon Safety Factor	MC: Mohr Coulomb	27.28 N/m^2	1.230×10⁶ N/m^2
TCP Safety Factor	VON: von Mises Stress	7.664 N/m^2	1.952×10³ N/m^2
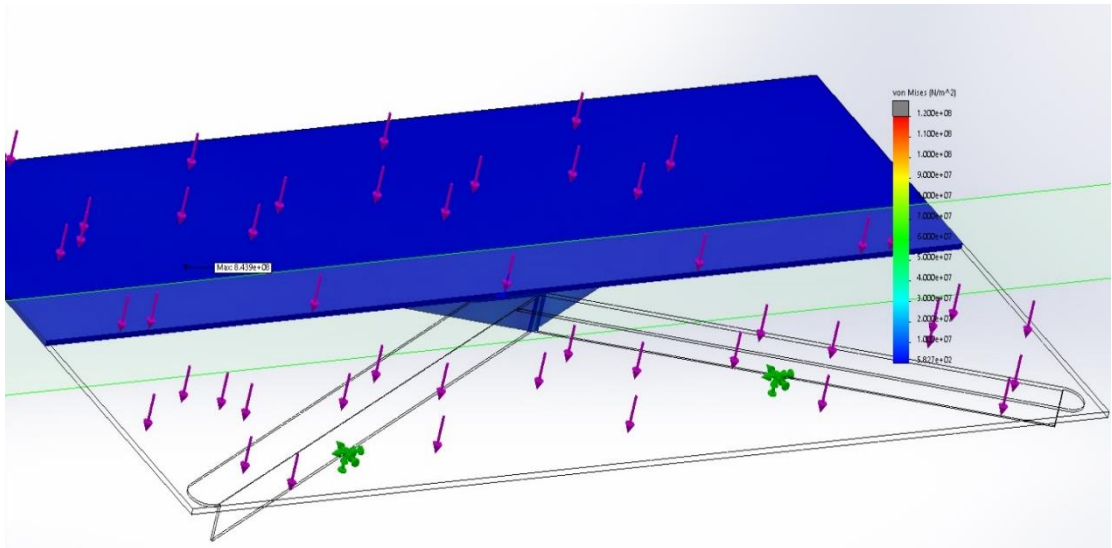
Figure 18 - Stress analysis under extreme wind load (section view)
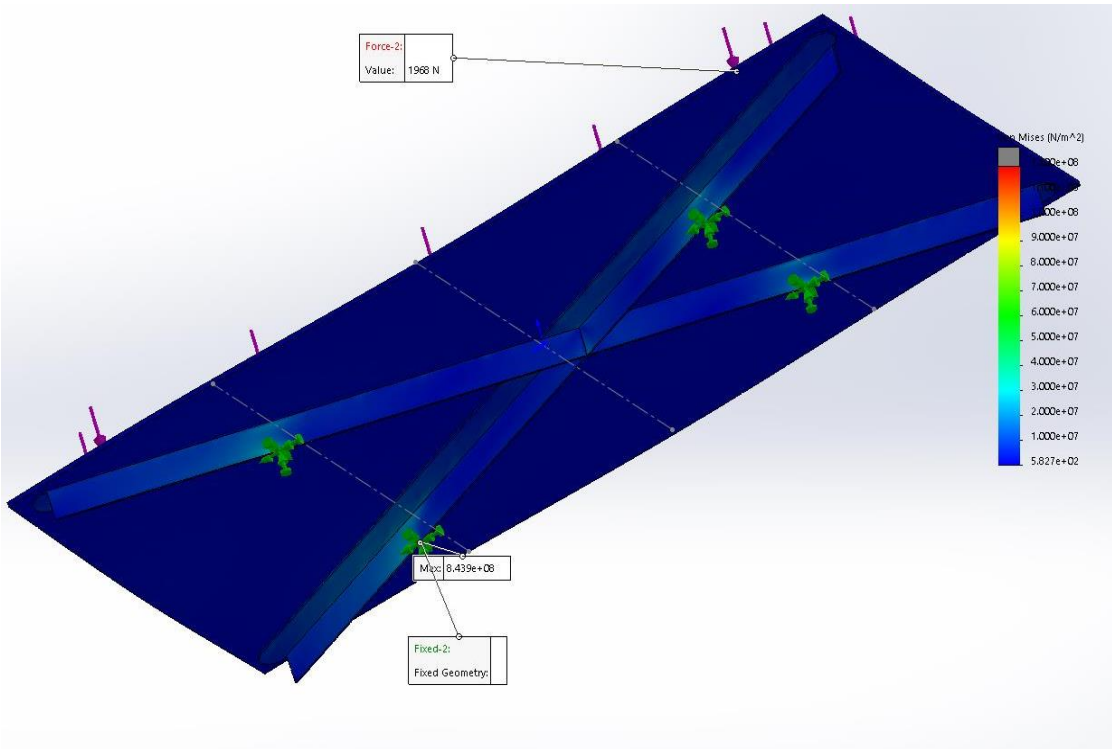
Figure 19 - Stress analysis under extreme wind load (X-frame)
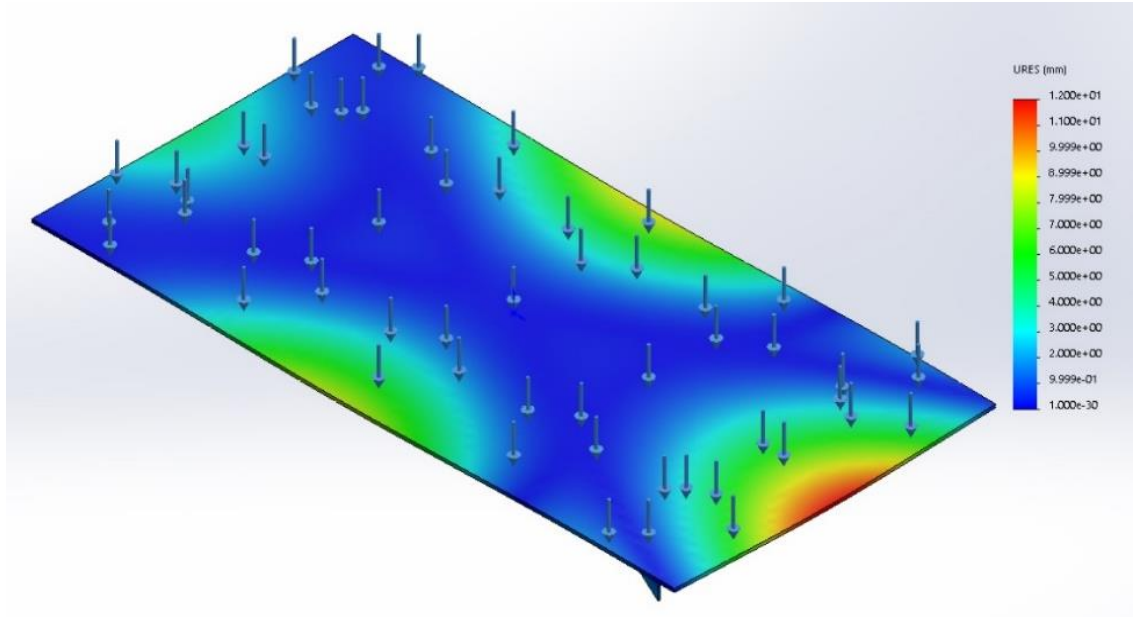
Figure 20 - Displacement analysis under extreme wind load (X-frame).

C. Weight Load Simulation

The stepping of a 90 kg person on a panel was approximated by normally applying 900 N to a 0.03 m^2 rectangular surface. Weight load was applied at one of the edges of the module where the panel is weakest according to the results of the wind load test (see Figure 21).
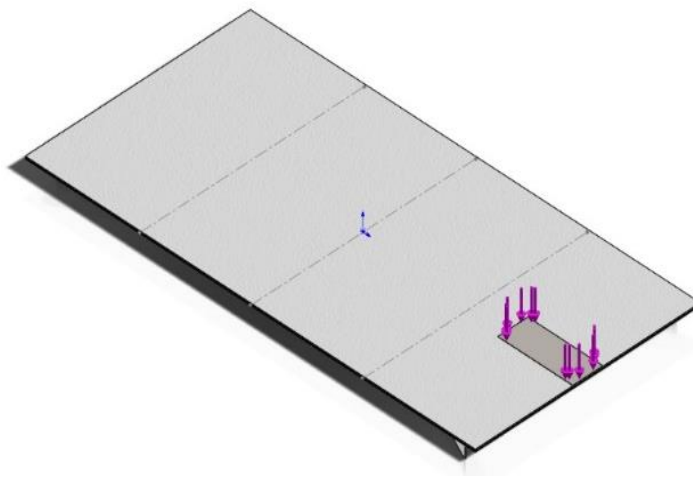
Figure 21 - Test weight applied at the edge of the panel.

Sufficient meshing was created in order to ensure the accuracy of the applied forces at the interface with the panel (refer to Figure 22).
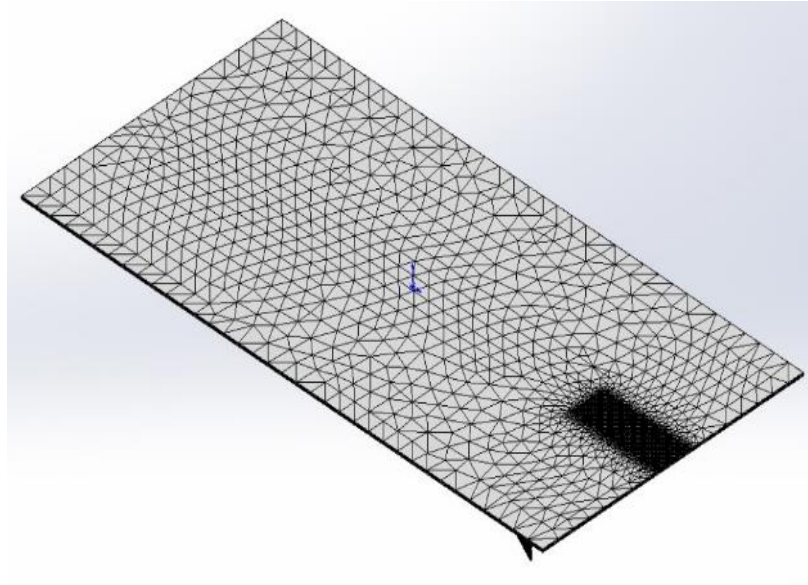
Figure 22 - Meshing with test weight applied at the edge of the panel.

Table 9 contains the weight application simulation results. Note that the total displacement is around 6 cm which is significant (see Figure 23). Visually and intuitively, one can safely assume that something in the structure is going to fail. The simulation results, however, show that safety factors allow for at least 57% increase in load. This is since one of the assumptions for linear computer-aided design CAD modelling was violated, namely, all deformations have to be elastic and small in relation to the dimensions of the model. Since this assumption failed, non-linear modelling with the appropriate material properties has to be applied. This, however, is outside of the scope of current dissertation, and the working assumption will be that the solar module will fail if stepped upon by an average American.

Table 9 - Weight load study results

Name	Type	Min	Max
Stress	VON: von Mises Stress	138.8 N/m^2	3.136×10^9 N/m^2
Displacement	URES: Resultant Displacement	1.000×10^{-30} mm	63.20 mm
Strain	ESTRN: Equivalent Strain	4.563×10^{-9}	0.1667
Acrylic Safety Factor	VON: von Mises Stress	1.827 N/m^2	2.275×10^4 N/m^2
PDMS Safety Factor	VON: von Mises Stress	2.210 N/m^2	6.604×10^3 N/m^2
Silicon Safety Factor	Mohr Coulomb	4.687 N/m^2	2.079×10^7 N/m^2
TCP Safety Factor	VON: von Mises Stress	1.572 N/m^2	1.601×10^4 N/m^2
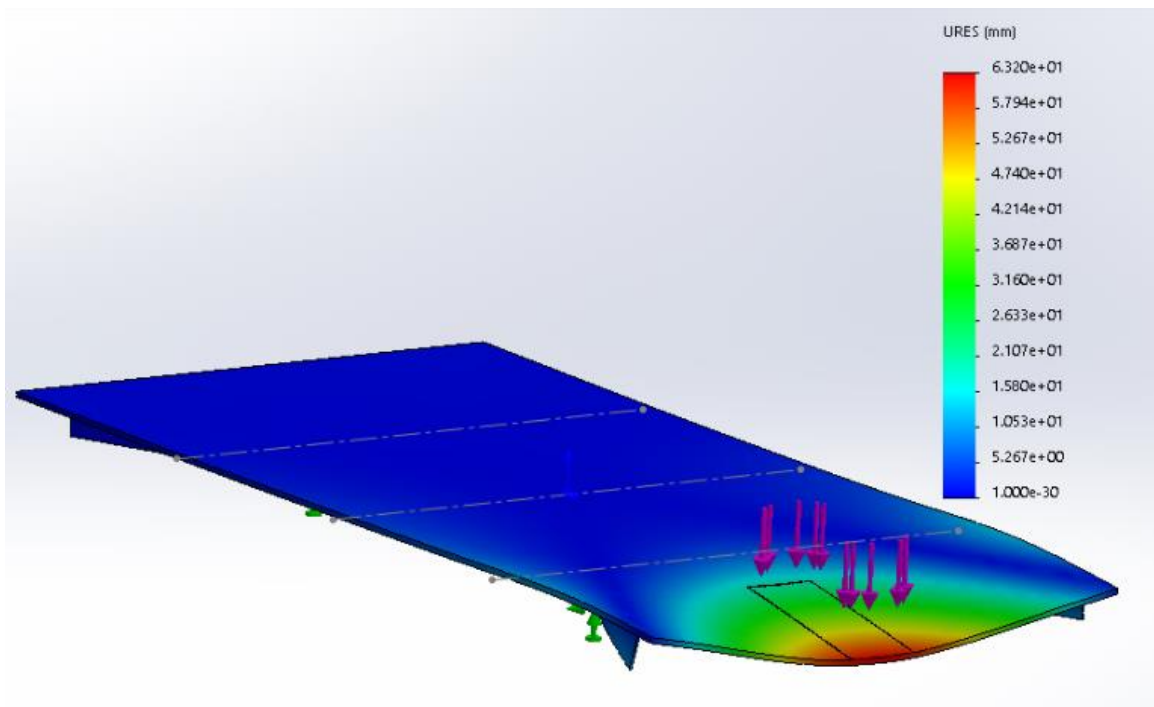
Figure 23 - Deformation under weight load.

VII. Heat Generation and ANSYS Thermal Modelling Results

Using Equations 5.1-5.4, it is possible to calculate reflected, absorbed, and transmitted lights in every media. Note that the equations are light frequency dependent, hence absorption coefficients for the materials used in conventional and proposed solar modules were collected from various sources [68], [69], [70], [71]. The above equations where then solved for each of these frequencies and the resultant energy absorbed by each layer for conventional and proposed solar structures are provided in Figures 24-25. For simplicity, once energy was reflected, it was neglected from the system. Note that the two graphs are almost identical, in fact calculations show that the difference between light absorbed by Si in a conventional and in the new structure are 370W and 371W correspondingly. Information on total heat generated by each layer is provided in Tables 10-11 Most heat generation is due to silicon in both cases.
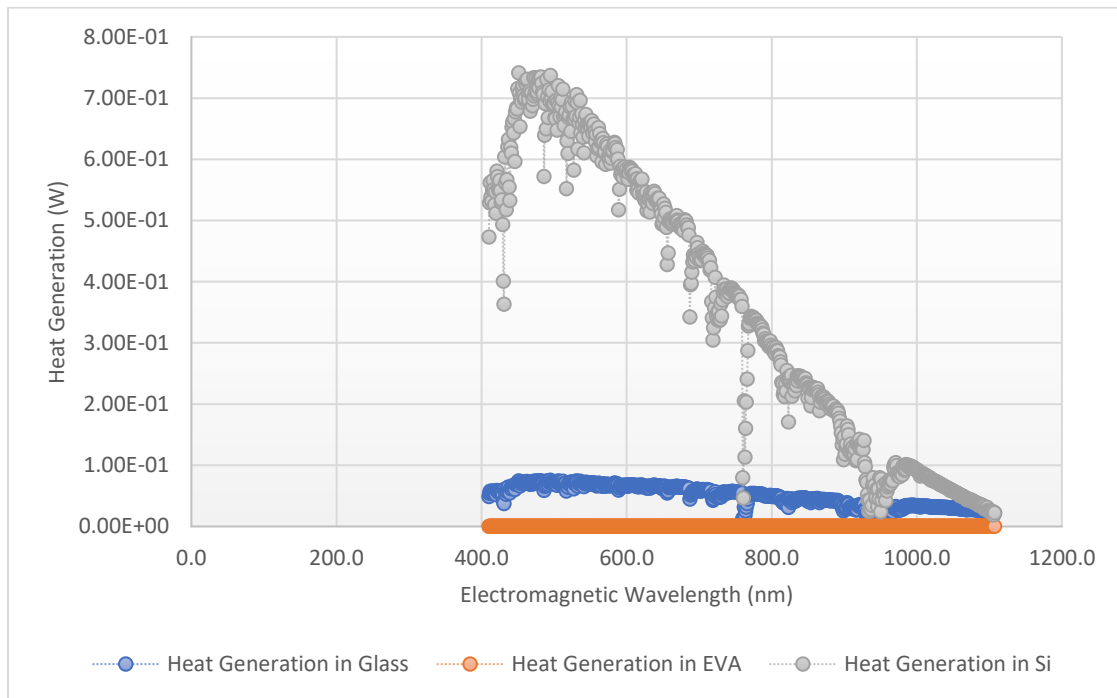
Figure 24 - Heat dissipation due to solar energy absorption in a conventional panel.
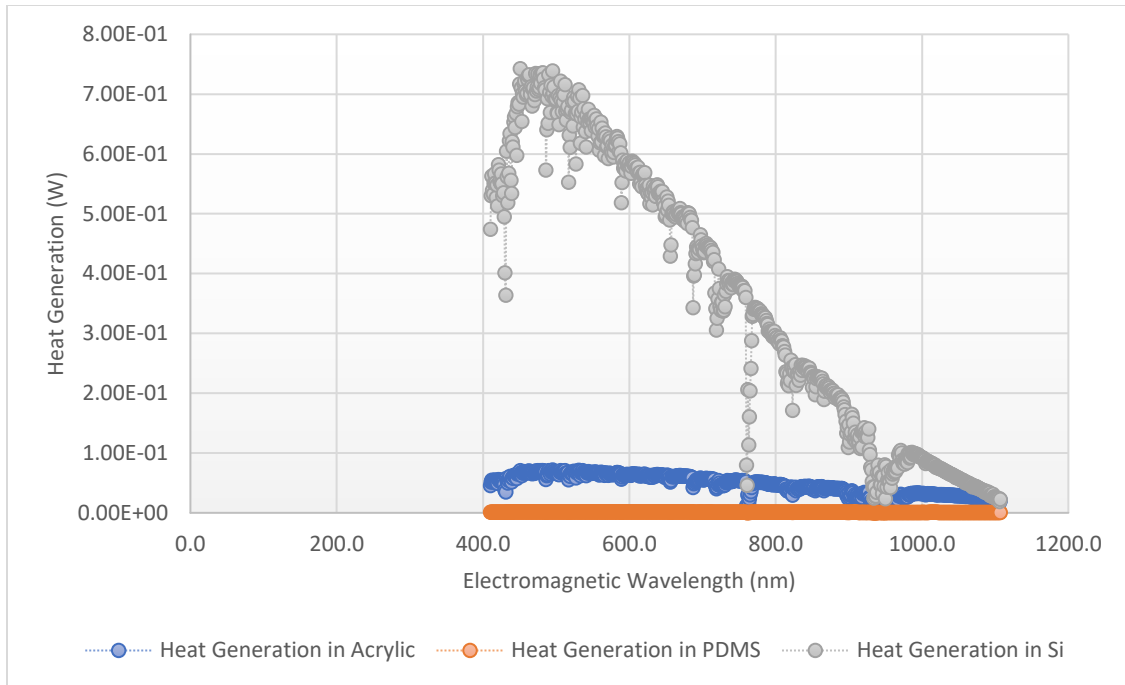
Figure 25 - Heat dissipation due to solar energy absorption *in a proposed panel.*

Table 10 - Heat generation by layer in a conventional panel.

Layer	Total Heat Generation Rate (W)
Glass	34.4
EVA	0.1
SiO$_2$	0
Si	245

Table 11 - Heat generation by layer in a proposed panel.

Layer	Total Heat Generation Rate (W)
Acrylic	32.8
PDMS	0.1
SiO$_2$	0
Si	246

These heat generation rate values are used in ANSYS thermal simulations as sources of internal heat generation. Equilibrium with the ambient room temperature is achieved due to convection from the front and back sides assuming no wind flow and internal heat generation rate. The convection effect was modelled using an air heat transfer coefficient of 15 $W*m^{-2}*K^{-1}$ for the front surface and a coefficient of 5 $W \times m^{-2} \times K^{-1}$ for the back surface. Ambient temperature was taken as 40˚C to test the panel under extreme hot conditions. ANSYS shows that the panel reaches thermal equilibrium at around 50˚C with the hottest region occurring in silicon's proximity (see Figures 26-27). Acrylic is rated for a continuous use at 80-90˚C and thus should be able to handle these temperatures.
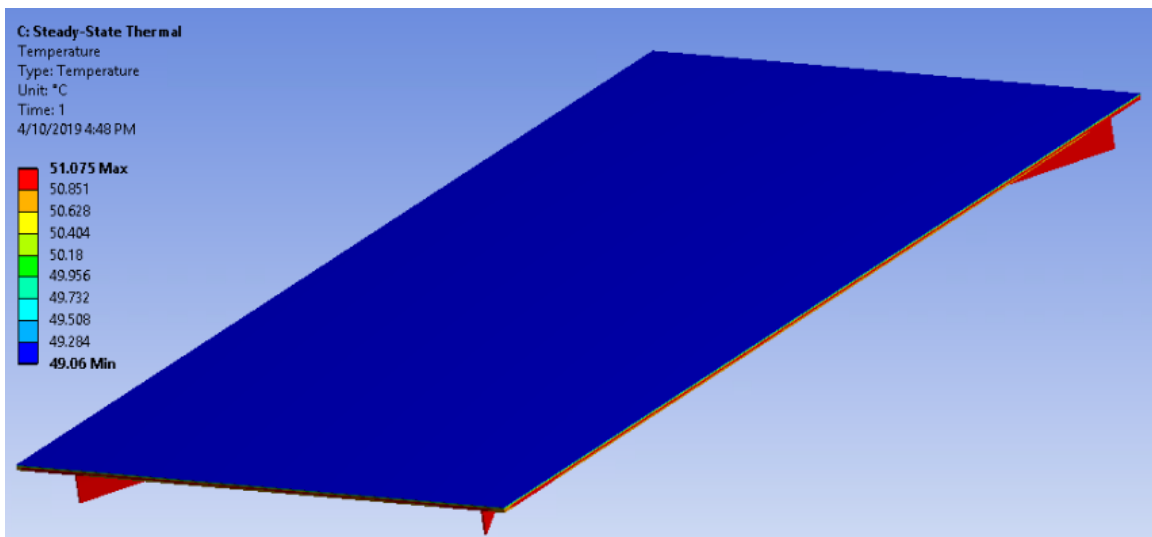
Figure 26 - Thermal simulation of a proposed structure.
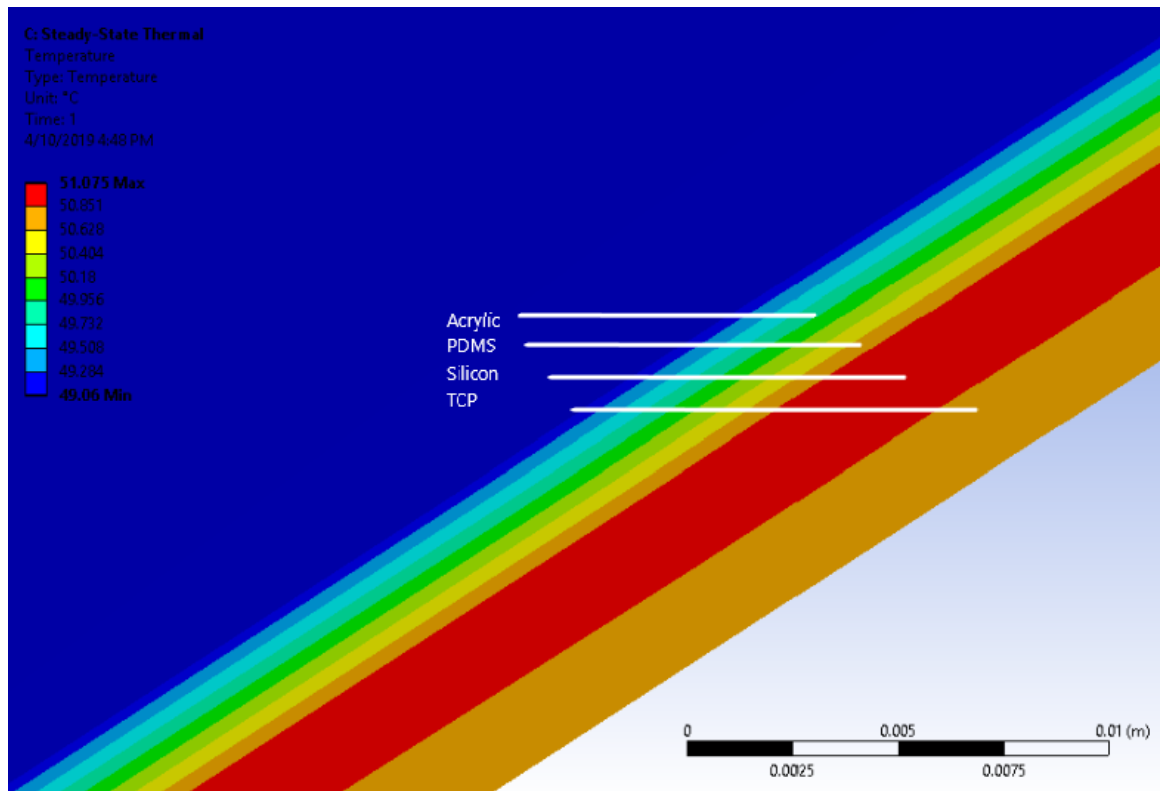
Figure 27 - Thermal distribution by layer.

VIII. Prototype Manufacturing

Initially, the PDMS material was attempted to be spin-coated onto a solar cell using the custom-made 3D printed rig. This method proved to be inefficient and unnecessary because of the surface tension of the material and the fact that it cures in 24-48 hours and would uniformly cover the surface of the cell on its own. It must be ensured, however, that the solar cell is lying flat and does not have any bowing as shown in Figure 28. Otherwise, this will distribute the PDMS along the edges of the cell, causing a ununiform coating. The first successful prototype is shown in Figure 29. It shows a single-cell module consisting of a polystyrene foam support, silicon solar cell, wooden frame to contain the PDMS encapsulant and the encapsulant itself.

54
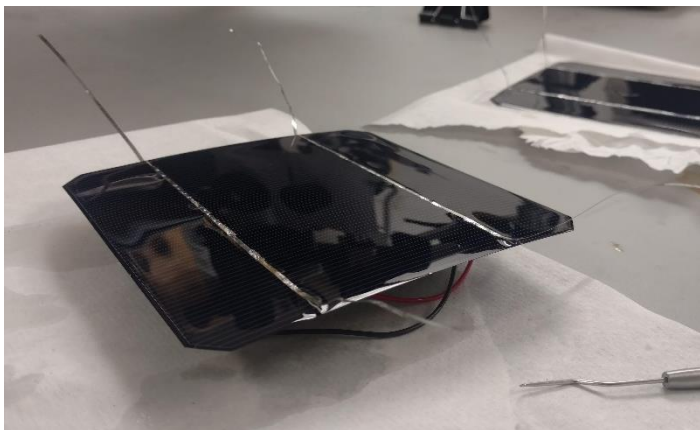
Figure 28 - First attempts in PDMS coating. Note the undesired bowing of the cell.

Figure 29 - PDMS-coated single-cell solar panel prototype

The thickness of the PDMS layer can be controlled by weighing the material (given the area of the application surface and mass density of PDMS). It soon became apparent, however, that the PDMS layer must have a surface cover because the dust and other small particles easily stick to the surface of the exposed PDMS. Hard-coated acrylic was chosen as a surface cover, due to its optical and mechanical properties, and the manufacturing steps of the assembly of the layers needed to be developed.

Several aluminum single-cell back plates were machined by our team with the dimensions shown in Figure 30. A test model with only an aluminum backplate, a solar cell, and PDMS encapsulant was built (refer to Figure 31).
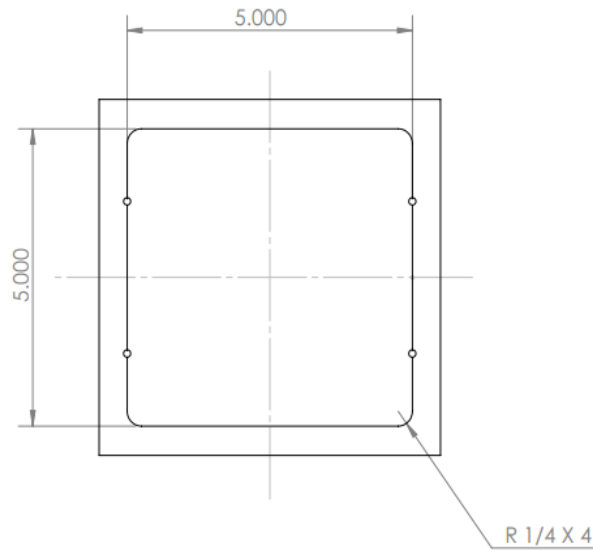
Figure 30 - Aluminum single cell backplate.

Figure 31 - Test prototype with an aluminum backplate.

Several failed attempts of PDMS crosslinking occurred during the manufacturing steps exploration. Initially, there were several instances where PDMS would not fully cover the space between the acrylic and silicon layers as shown in Figure 32. This was partially caused by the acrylic-aluminum misalignment and partially by trapping of air bubbles during PDMS cross-linking. An aspirator chamber from the Chemical Department was used to degas the PDMS during the initial half an hour of the curing process. Some improvements were observed, so a higher vacuum curing environment (-25" Hg) was also tested using a vacuum chamber available in the ETIC building. The results were not significantly different from before, however the combination of the acrylic aligners and small constant pressure application seemed to give the best result.
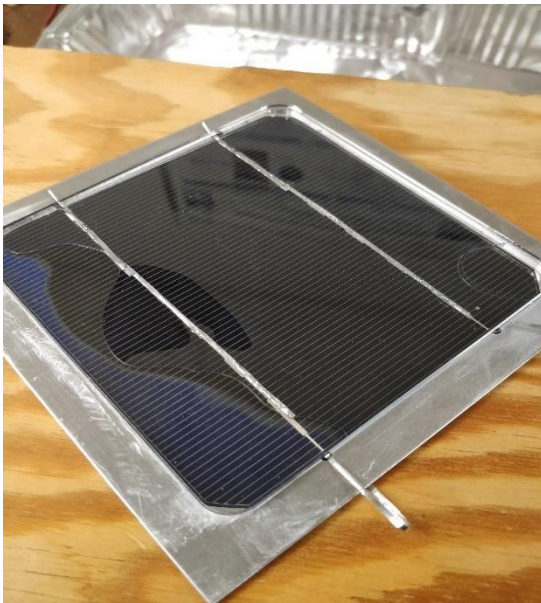
Figure 32 - Failed encapsulation sample.

Figure 33 - Aggressive bubbling due to curing under high temperatures

In order to facilitate the curing process, it was suggested by the Dean of Plastics Engineering to increase the ambient temperature, apply pressure (to about 50˚C, 30 lbs),

and let it sit overnight. Plastics Engineering department has a heated press which was perfect for this test. The result is shown in Figure 33, and unfortunately the proposed method did not work out well. Our speculation is that because the curing time shortens, air bubbles have much less time to be released from the edges of the panel, and as a result they get trapped inside. When the procedure was reverted back to the room temperature curing, under small pressure, while ensuring that the acrylic and aluminum pieces aligned, the best prototype results were acquired (refer to Figure 34). These results might improve even better, if it is done in a high vacuum environment. Additionally, overall bad adhesion between PDMS and aluminum were observed, presumably due to the shiny surface of the aluminum, which would not be such a big issue with TCP.

Figure 34 - Single-cell solar panel prototype with the PDMS and acrylic layers.

IX. Conclusion & Future Work

Calculations and computer models of a potential new design of solar modules indicate the prospective of having 20% lighter solar panels which translates into many initial cost savings as well as long run operation costs due to savings in the energy required for tracking. Many simplified assumptions were made, however, that need to be further verified. First, acrylic is much more vulnerable to abrasion effects when compared to glass; there exist, however, hard coated acrylic variations that need to be evaluated for reliability of operation under harsh outdoor conditions. Second, PDMS is already used in industry as an encapsulant [50], [51], [52], however our prototype tests showed poor adhesion between PDMS and the adjacent layers. This is presumable due to improper curing conditions or base-to-catalyst ratio, but more experiments are needed to establish the exact reason and address it. Although CoolPoly D3612 TCP claims to be widely used for many outdoor applications, it is based on the Nylon 6 polymer which is subject to a certain percentage of water absorption which might affect its degradation rate and thus needs to pass through an accelerated wear test. The overall structure of the model needs to be adjusted for the optimal manufacturing processes to decrease its cost. However, this chapter shows that the preliminary manufacturing steps seem to consist of simple steps, the design might be adjusted to match the existing mounting infrastructure and is retrofittable, and the new module's thermal, optical, and structural properties are comparable to the existing designs. All these factors as well as the fact that the module's weight that is only 80% of current design can make certain marginal solar projects cost-effective and earn its own place on the market.

CHAPTER VI. ANTI-TRACKING CURTAILMENT ASSISTANCE SYSTEM

I. Problem Statement:

Solar renewable energy production peak does not match with peak demand during a typical day. Ever increasing solar energy penetration poses a significant power overproduction and grid operation stability problems. Many solutions to address this are offered but need time to mature. Meanwhile, solar energy curtailment is often used. Solar energy curtailment is not an ideal option and has monetary and operation costs associated with it. Anti-Tracking, solar energy curtailment by controlling solar incidence angle, could improve solar energy curtailment implementation because the system input energy is reduced before it reaches both the panels or inverters and thus significantly reduces maintenance costs. Additionally, Anti-Tracking is retrofittable to the existing solar plants with tracking mechanisms and thus require little time to be deployed.

II. Introduction

Solar renewable energy production peak does not match with peak demand during a typical day. Ever increasing solar energy penetration poses a significant power overproduction problem and grid operation stability [72], [73], [74], [75], [76]. Many solutions to this problem are offered and discussed in the industry, however the majority of them need time to mature or reach the point when they are cost-effective. One of the currently used temporary solutions to address this problem is solar energy curtailment. Solar energy

curtailment is often not an ideal option and poses significant monetary and operation cost implications. Uncertainty associated with curtailment increases project financing costs and thus energy cost; curtailed energy dissipates in smart inverters and solar panels. Inverters are shown to account for 37% of unscheduled maintenance repairs and 59% of unscheduled maintenance costs [42], [72], [77]; these figures are likely to increase when the curtailment strategies are implemented. In some cases, however (high PV energy presence, low grid interconnection), the curtailment strategy lacks better alternatives. This dissertation discusses how Anti-Tracking can improve solar energy curtailment implementation. Anti-Tracking is a calculated turning of solar panels away from the sun when the solar production reaches a power threshold either pre-set by an operator or sent real-time from the grid. Anti-Tracking is expected to reduce plant-level power losses associated with heat dissipated in smart inverters and solar panels operating at non-MPP (non-Maximum-Power-Point) because the system input energy is curtailed before it reaches either panels or inverters. Combining solar Anti-Tracking and Tracking modes, it is possible to increase energy production during early and late hours of the day and "follow" a statically set or dynamically updated power threshold value during mid-day. Considering the expected energy curtailment mid-day, an increase of early and late hours daily energy production is a significant factor. Anti-Tracking is expected to be retrofittable to existing solar plants with tracking systems (either single- or dual-axis). The added benefit of anti-tracking in solar plants that oversize their inverters will be discussed. An anti-tracking system implementation outline will also be provided in this chapter.

III. Current Trends and Future Challenges

Solar energy generation prices are fuel-free and are largely driven by the initial investment costs and financing. PV module prices have been consistently following a 28.5% price drop for every doubling of installed capacity since 1976 (refer to Fig. 35). In 2017-2018, new global solar installations were 99 GW and 109 GW respectively (2018 data is estimated as of Jan 16, 2019, refer to Fig. 36). Historical upward trend of new annual PV installations is likely to continue to grow. According to Bloomberg NEF, solar and wind will account for 50% of energy production worldwide by 2050 [1].
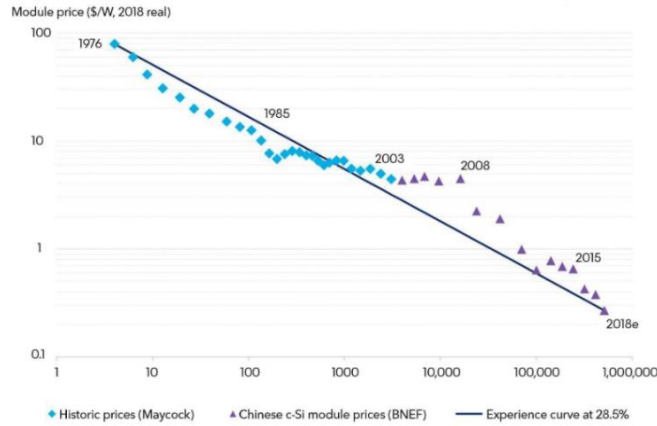
Figure 35 - PV module historical price drop data [1].
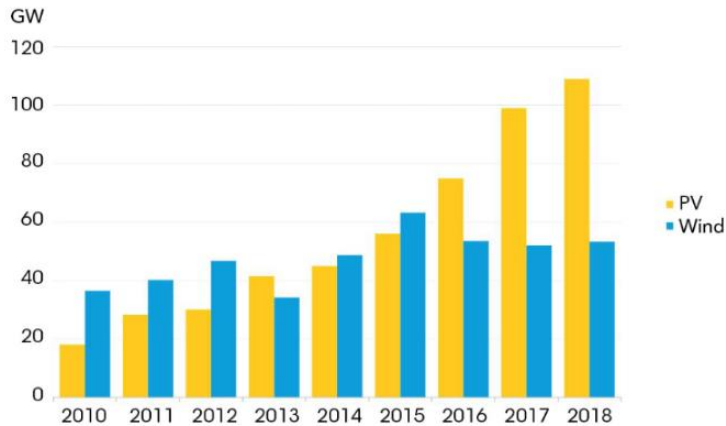
Source: BloombergNEF. Note that the capacity added figures in this chart are preliminary estimates.

Figure 36 - New global wind and solar PV installations [78].

Solar energy generation has three important characteristics associated with it: it is intermittent, hard to accurately predict, and its peak generation time of the day does not correspond with typical peak demand time. This poses some significant challenges to the electric grid and the goal of achieving fully renewable energy generation. This section of the chapter will give an overview of the origins of these challenges which are related to daily energy demand patterns, different characteristics and flexibility of energy generation technologies, and solar energy generation patterns.

First, the daily energy demand curve follows a somewhat predictable shape that is caused by typical hourly human activity patterns. For a given location, energy demand is lowest at night when everyone is asleep. A local peak occurs at around 7-8 AM when people start to wake up and prepare to leave for work. Daytime energy demand is lowest at around 1-3 PM presumably due to lower need for artificial lighting, and absolute energy demand peak occurs at 7-8 PM when most people are home and actively use electricity after dusk. Figure 37 shows a real demand curve in New England on February 1, 2019 provided by New England ISO (Independent System Operator) and shown here as an example.
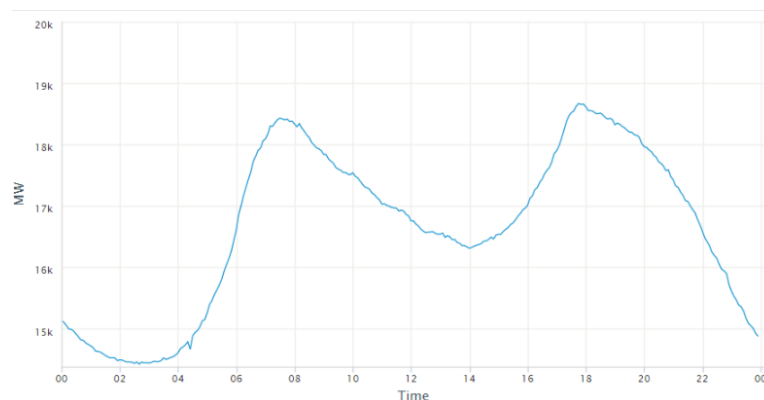
Figure 37 - New England energy demand sample data (Source: NE-ISO's online grid tracker, February 1, 2019)

Second, in order to meet this demand, a local system operator uses different strategies to schedule energy generation by different sources depending on factors such as the season, weather, time of the day, and real-time demand data. The details of this process will not be described in this work, however the basic principles are provided below. Energy generation by type can differ in four main characteristics: merit (how clean it is), cost, ramp time (how fast it can be brought up to full capacity energy output), and typical capacity factor (how much energy can a given source supply). Nuclear energy, for example, is clean, has a reliable power output with an average cost, but has the lowest ramp rate compared to other sources. Thus, usually nuclear energy covers what is known as "base load", the highest constant energy level that is in demand at all times (which constituted 20% of energy in 2017 [4]). Coal and gas have relatively high generation reliability and thus are often used as dispatchable energy sources to balance supply with demand at all times, but they produce the most carbon emissions and thus supply energy where renewables cannot meet the demand (29% and 32% of total energy supplied in 2017 correspondingly). Renewable energy sources such as solar and wind, although very cheap and clean, are less reliable and time-specific. Renewables are generally expected to produce less that their nameplate capacity within a day which is taken into account when planning an energy dispatch strategy by the system operator. A full description of the energy characteristics by generation type are provided in Table 12 from [79].

Table 12 - Energy characteristics description by generation source [79]. CCGT – closed-cycle gas turbine (same water is recirculated in the system); OCGT – open-cycle gas turbine (fresh water is supplied to the system and then discharged to the atmosphere); PV – photovoltaic; CSP – concentrating solar plant; LCOE – levelized cost of energy (ratio of the total cost to build and operate a plant over the total energy produced by the plant during its lifetime).

Generation Type	Typical Capacity Factor	Maturity	Start-up time (hours)	Typical LCOE ($/MWh)	Capital Cost ($/kW)	Typical Ramp Rate (% Full load / Minute)	Typical Life-Cycle Emissions (g CO2e / kWh)	Availability Factor
Coal	53 - 85%	Mature	1.5 - 3	72 - 105	3900 - 3950	6	933 - 1048	> 80%
Gas CCGT	56 - 87%	Mature	01-Feb	30 - 36	1050	8	411 - 487	> 80%
Gas OCGT	8 - 30%	Mature	0.1 - 0.2	69 - 122	900	20	543 - 692	> 80 %
Oil	~ 8%	Mature	3	Not Available	~ 400	7	530 - 900	> 80%
Diesel	66%	Mature	< 0.01	200 - 280	500 - 800	25	800 - 1056	89 - 91%
Nuclear	92%	Mature	24	63	6070 - 6200	2	07 - 25	80-90%
Biomass	56%	Deployment	3	107 - 109	3940 - 4100	8	18 - 59	
Solar PV	15 - 27%	Mature		35 - 81	1770 - 1780		37 - 50	97-99%
Solar CSP	44 - 60%	Deployment	2.5	95 - 167	7840	6	16 - 37	
On-shore Wind	11 - 48%	Mature		22 - 169	1520 - 1750		8 - 20	95 - 99%
Off-shore wind	31 - 51%	Mature		95 - 268	3780 - 8200		10 - 15	95 - 99%
Hydro	60 - 66%	Mature	< 0.1	35 - 70	3960 - 7410	15	4 - 15	80 - 90%
Tidal	~ 25%	Demonstration		230 - 250	3300 - 3600		06 - 11	95 - 98%
Geothermal	80-90%	Mature	1.5	76 - 237	5100 - 13670	15	17 - 57	92 - 99%

Third, the solar energy generation curve has a bell shape and it peaks at noon where the energy demand is relatively low. This is the root of the problem currently associated with PV energy generation and is best illustrated with California's well-known "duck curve" (refer to Figure 38). The figure illustrates California's net load on a typical spring day where the fraction of the predicted net demand met by solar and wind is subtracted from the expected total net demand [80]. Thus the "belly" of the curve shows that with ever increasing presence of solar energy in the grid, there likely to be a point where the total

supply of energy will be higher than the total demand which might cause significant disturbances to power quality and grid reliability. This as well as overall increase of solar renewable energy in the energy mix worldwide calls for new ways of increasing grid flexibility [73], [74], [75], [80].
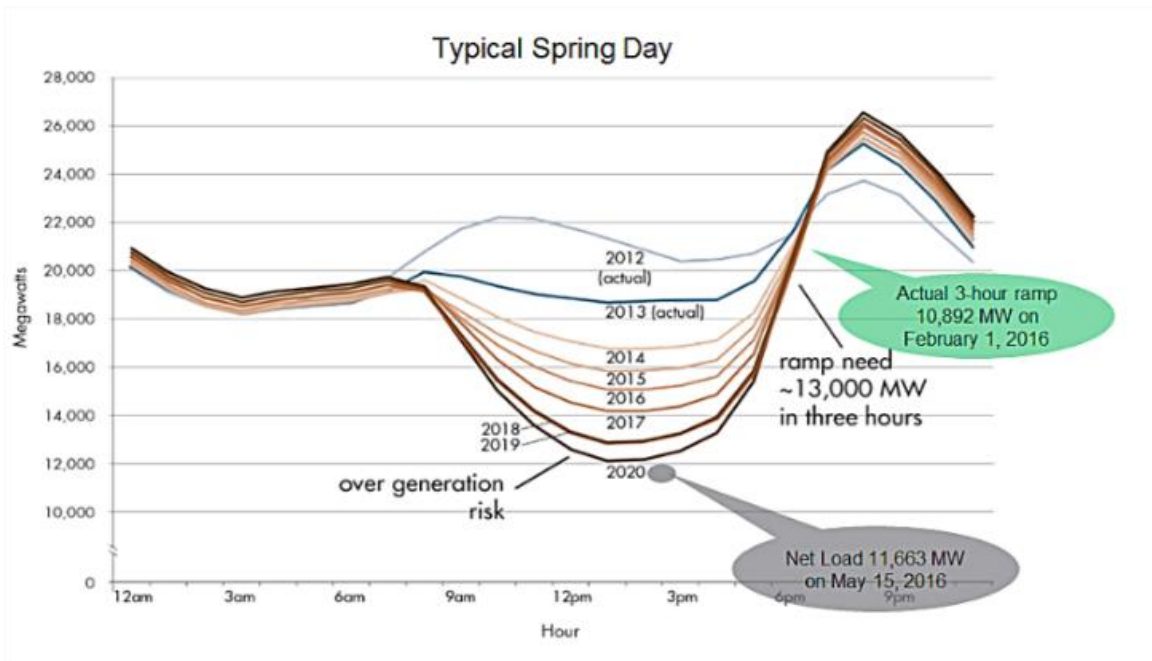
Figure 38 - California's "Duck Curve" [80].

IV. Solar Energy Curtailment

Ultimately, the solution of this problem is likely to be the increase of energy storage resources that can absorb energy during an overproduction period, supply it during peak demand periods, and make renewable energy sources such as wind and solar dispatchable. According to Bloomberg NEF estimates, Li-ion battery prices will fall by 66% between 2017 and 2030 [1]. Currently, however, battery storage technology is not considered to be cost-effective in majority of the PV system installations. As of 2018, there is 1.6 GW of energy storage installed in US (excluding pumped-hydro) [75] compared to 60 GW of solar

installation [76]. By 2021, solar PV installations are expected to reach 100 GW in US [76], and battery storage is expected to grow 2.5 times worldwide [1]. Meanwhile, solar energy curtailment is among some of the currently available strategies to address the overproduction problem. Although, solar energy curtailment is often used as an absolute last-resort, under certain conditions and in small scales it might be the most cost-effective solution [73], [74], [81], [82]. California currently curtails up to 4.7% of solar energy depending on the month (although usually 1.5-2.5%). This is calculated from California-ISO's monthly reports [83]. Other strategies to address energy oversupply include demand-side management, higher grid interconnectedness, and more accurate renewable energy generation predictions. The purpose of this work, however, is not to prove that solar energy curtailment should be used more often or that it is more cost-effective (which is often not the case), rather to improve the solar energy curtailment execution when it is sought to be used.

V. Financial Aspect of Curtailment

Solar energy curtailment also has policy related challenges associated with it and they are best demonstrated in the case of Hawaii, where unique circumstances best emphasize these challenges. Hawaiian curtailment policy challenges and proposed solutions are described in the study from ScottMadden [73] and are briefly described next. Hawaii has a lot of solar resource which pushed the increase in PV installations. The state's grid system only powers itself and cannot export the excess energy, thus the need for PV energy curtailment is present and is only expected to grow. Figure 39 depicts the Hawaiian Electric Companies' projections of energy generated by different sources, and the pink region indicates

overgeneration. Note, that as wind (green) and solar (yellow) energy contributions grow, other sources are reduced; yet the energy overgeneration only increases.

Curtailment in such significant amounts raises questions regarding the curtailment policies and proper curtailment compensation. PV generation plants have significant investment costs and limited lifetime (typically 20 years), so all energy that is curtailed is considered lost profit. Currently, energy producers are compensated only for the energy that is supplied to the utility, but due to the unpredictable nature of curtailment in large scales, it raises project-associated risks and therefore the financing costs, which in turn raises electricity costs for the end user. However, if the energy producers were to be compensated for the energy delivered as well as energy curtailed, this will also increase the cost of electricity. ScottMadden indicated this problem in their report [73] and suggested three alternative ways to take solar curtailment into consideration with an optimal pricing for both the end users and energy producers. The first method consisted of two different payments: capacity (guaranteed base payment) and energy (payment that depends on how much curtailment occurred in a given period). The advantage of this method is that it guarantees a certain consistent amount of payment to the power producer which decreases the level of project uncertainty. The second method consists of time-of-day price caps or coefficients. This method integrates curtailment into energy generation in a clear way,
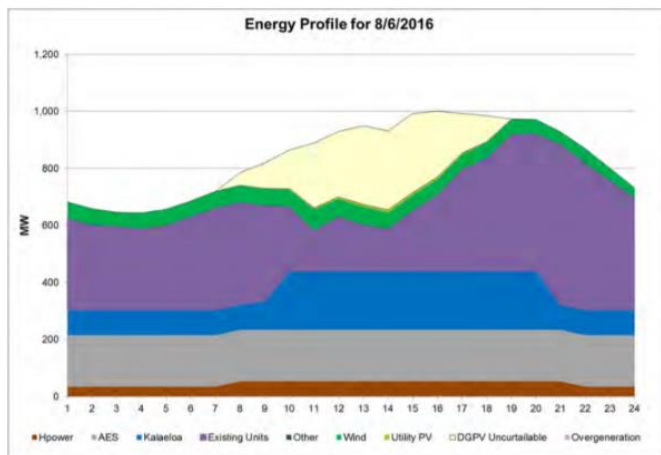
(a)
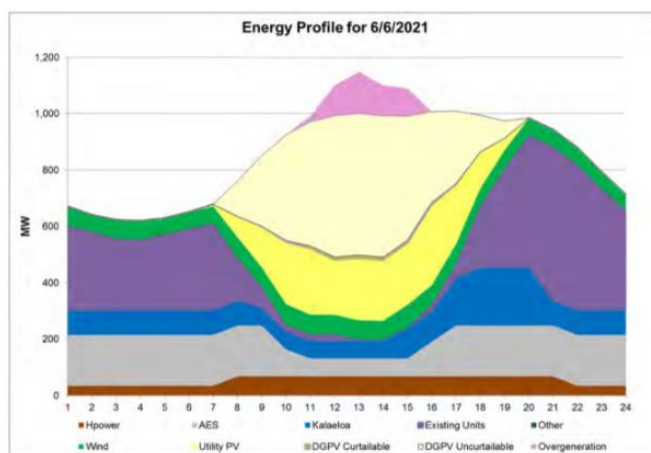
(b)
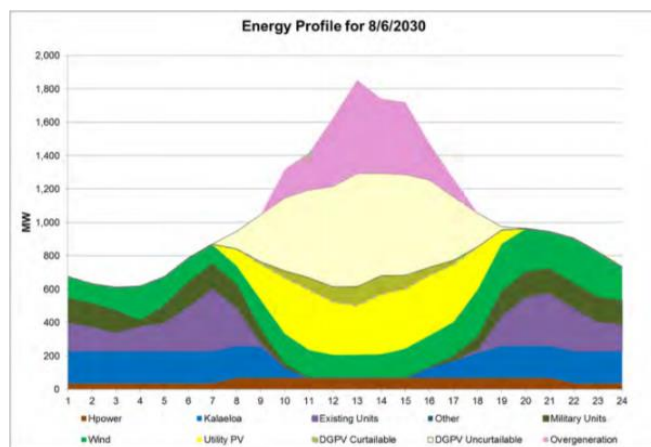
(c)

Figure 39 - Share of renewable energy and overgeneration in Hawaiian electrogrid (estimation) in a) summer 2016, b) summer 2021, c) summer 2030 [84].

where the compensation for energy produced depends on the time of the day and is known to market participants ahead of time. With this method, energy generation mid-day can be disincentivized by low or negative payment coefficients and the market participants can determine their energy production strategy ahead of time and for a long term. The third strategy consists of using solar energy as dispatchable source. This can be accomplished by allocating a certain portion of energy production capacity only for a dispatch purpose when energy production disturbances occur in the grid as a whole (i.e. active and reactive power regulation [73], [74]) and pay a service payment for ancillary services provided.

VI. Equipment Degradation

There is also an increased risk of premature equipment degradation when a solar energy curtailment strategy is employed. This section will describe the origins of these additional equipment strains and show how anti-tracking can help resolve these issues. A typical solar inverter consists of two stages: DC-DC converter for MPPT and the final DC-AC stage (refer to Fig. 33 from TI).
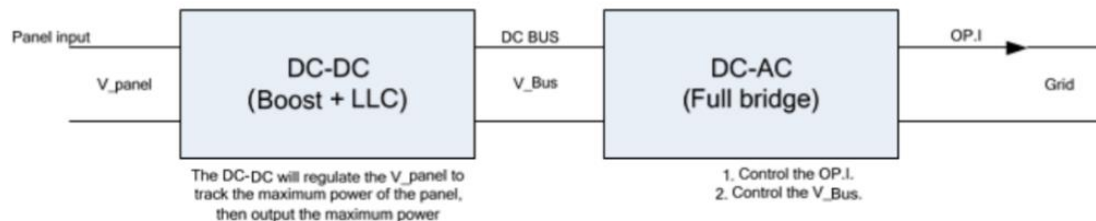
Figure 40. Typical DC-DC converter block diagram [85].

The first stage is needed to introduce a proper input impedance in order to get the maximum power out of the solar arrays. This stage is unlikely to be affected by the curtailment

realization process because if one was to realize power curtailment by operating the solar panels at non-MPP, the excess energy would have dissipated inside the solar panels and degrade their performance and long-term operation. Thus, it is more likely that the solar curtailment will be realized in the following DC-AC stage, however, sometimes there might be an intermediate DC-DC stage. Regardless, the converters employ switching power FETs and control output power by varying either duty cycle or modulation index (the range in which the duty cycle changes). Note: in a traditional asynchronous design of a DC-DC converter, the excess energy would have been dissipated in a power diode. However, in high power applications, synchronous converters are preferred where the power diodes are replaced with switching power FETs that are powered with a complementary duty cycle with some dead-time, t_{dead}, to avoid shoot-through current [86], [87]. Switching dead-time increases when the solar energy is curtailed inside of a power converter (either DC-DC, DC-AC, or both) and it has some power losses associated with it (refer to Equation 6.1).

$$P_{loss} = V_f \times I_o \times t_{dead} \times f_{switch} \qquad (6.1)$$

where P_{loss} is power dissipated in the FET during dead-time, V_f is the forward bias voltage of FET's body diode, I_o is output current, and f_{switch} is switching frequency.

This formula is very similar for both hard-switching and zero-volt-switching circuits. The use of soft-switching circuits is recommended for high-power applications, however [88], [89], [90], [91]. All this excess energy heat dissipations in FETs decrease their lifetime and might significantly affect the Operation and Maintenance (O&M) costs of the inverters.

This is important because according to a five-year study case of a utility-scale PV system, inverters accounted for 37% of unscheduled maintenance events and 59% of unscheduled maintenance costs [72]. According to a report from ScottMadden, inverters account for 62% of PV system component failures and around 37% of energy loss [77]. These numbers are likely to grow when the solar energy curtailment strategy is employed. Hence, anti-tracking is suggested as a tool for executing solar energy curtailment so the energy is reduced even before it enters the solar panels and thus will not damage either the panels or the expensive smart inverters.

VII. Technological Realization

Smart solar inverters are already designed to both communicate with the grid and perform solar curtailment through the internal power dissipation [2], [92], [93]. They are also popular in industry; according to [94], almost half of the utilities that are 2015 survey respondents said that they are either already implementing or considering an advanced inverter project. Many ancillary service capabilities are already in-built into the smart inverters, they can be activated remotely, and the direct costs of these functionality implementations are small [94]. Anti-tracking should initially be a secondary curtailment tool that follows the solar inverter curtailment, and its role should be the reduction of power dissipated in the solar smart inverter.

The smart inverter can either have the max power output threshold pre-programmed or sent to it by the grid operator. Figure 41 shows a diagram of such a technology infrastructure offered by SMA [93], one of the largest PV equipment companies. The signal from the grid
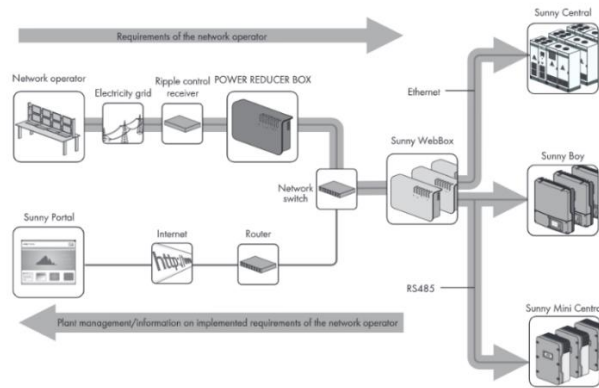
Figure 41 – SMA's grid-plant communication technology infrastructure [134]

operator is sent as harmonics through the power transmission lines. It is then decoded by the Power Reducer Box and the interpreted signal is then sent to the solar smart inverter through the Sunny WebBox interface. In order to synchronize the turning of solar panels and solar power curtailment that occurs in the solar smart inverters, it needs to be ensured that the communication between the inverter and PLCs is possible. Companies like Satcon Inverter Solutions provide open communication interfaces to read and/or write registers of their smart inverters using industry-standard communication protocols [95]. These protocols are supported by PLCs allowing them to read the live power output values (registers 30087, 30088, 30089) as well as the max power output threshold value (register 30103) [95]. This information should theoretically be enough to perform a simple Proportional–Integral–Derivative (PID) control for the solar power threshold-tracking (also known as anti-tracking). PLCs control the solar panel tracking position through

Variable Frequency Drives (VCFs) connected to AC motors, or through DC drives connected to stepper motors. A high-level programming language called "Ladder logic" is used to program PLCs. PID control is easily realizable in PLCs because a "PID module" is one of the standard command modules in a standard PLC command library. It is used by specifying the proportional, integrational, and differential coefficients, which are strongly dependent on the particular mechanical system.

VIII. Implementation Analysis and Relevant Concerns

The curtailment is achieved due to two independent factors: decrease in the effective area of the solar cell as well as the increase in solar energy reflection. The first loss mechanism can be calculated using simple trigonometric principles and is equal to the cosine of the angle of inclination. The second loss mechanism can be estimated using solar light reflection calculations based on the incidence angle like the ones provided in a study by Soga and Alasaka [96]. Figure 42 shows a MATLAB code used for plotting the combined effect of these two independent curtailment mechanisms. The first line defines the controlled variable (the inclination angle in degrees), the second line is the coefficient of light transmitted to the solar panel (the data is sampled from a graph in [96]). These numbers are the coefficient of light transmitted to the panel (as opposed to reflected) at the corresponding incident angles from the first line. The third line calculates the effective area of the panel and multiplies it with the light transmitted to the panel at any given inclination angle. This coefficient of energy collected is then plotted and the result is shown in Figure 43. The profile of the curve can be approximated as linear while there is a shallower slope at the small inclination angles. This is probably a positive characteristic because the system

will not be easily disturbed from its equilibrium position at a normal incidence angle during regular operation. At that point, however, the PLC settings for the PID control are likely to play a predominant role in the responsiveness characteristics of the system to sudden changes in the environment.

```
inclination_angle = [0:5:90];
light_transmitted_to_panel = ...
    [0.87, 0.87, 0.87, 0.87, 0.87, ...
     0.86, 0.86, 0.85, 0.85, 0.84, ...
     0.83, 0.81, 0.78, 0.71, 0.65, ...
     0.55, 0.40, 0.22, 0];
coefficient_of_energy_collected = ...
    cos(pi*inclination_angle/180).*light_transmitted_to_panel;
plot(inclination_angle, coefficient_of_energy_collected)
```

Figure 42 - MATLAB curtailment sensitivity estimation code snippet.
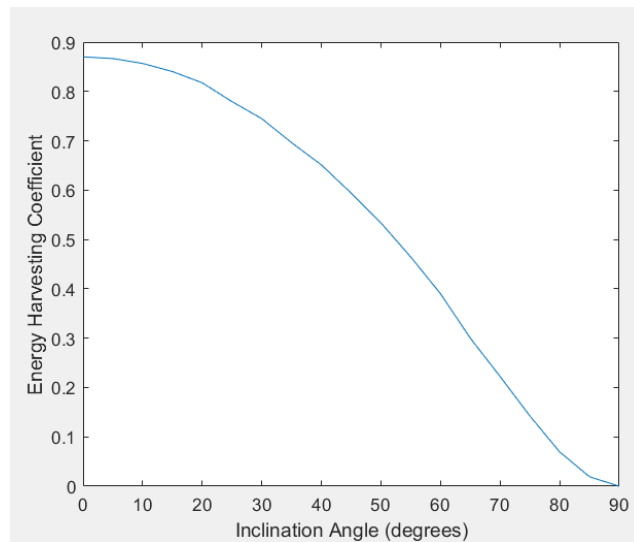
Figure 43 - Energy Harvesting Coefficient vs. Panel Inclination Angle

The role of anti-tracking is to cut the bulk of energy that would have otherwise been dissipated in the inverter. There should also probably be some small amount of energy that is dissipated in the inverter all the time to give the PID control some time to react when there is again an undersupply of energy.

There are also some concerns that are related to the feedback between the anti-tracking curtailment and the MPPT algorithm built-into the inverters. Theoretically, MPPT algorithms should be able to track the maximum power point of the solar panel strings with or without the anti-tracking assistance tool installed, however they might not have been tested for sharp energy output changes that would be expected with anti-tracking.

IX. Summary

This chapter looked at the present context for solar power curtailment and future perspectives. Due to the continuingly increasing presence of renewables in the power grid, and certain challenges associated with many power overproduction problem solutions, it is reasonable to expect growth in solar energy curtailment. Present approaches for solar curtailment are almost exclusively reliant on the dissipation of excess energy through expensive smart inverters which will poorly affect profits in the long run. Mechanisms of equipment degradation processes were also explained. This problem can be alleviated by introducing an anti-tracking curtailment strategy to the plant's operation if it already has a tracking system in place. With a simple modification of the existing infrastructure and minimal changes introduced to the hardware, it is possible to curtail solar energy by turning solar panels away from the sun when needed. This reduces the power that gets into the system, so minimum energy dissipation happens inside, and equipment lifetime is less affected. It is possible to modify an existing solar tracking algorithm with a possibility of setting upper and lower thresholds (inverters usually have a minimum allowed voltage rating) and a PID control run by PLCs.

CHAPTER VII. CONCLUSION

The solar energy industry is currently booming and is likely to continue to grow at very high rates. This trend is increasing the need for photovoltaic system optimizations on multiple levels in order to achieve higher profit margins and further procure solar energy systems deployment. This dissertation suggests several technological and procedural changes in solar photovoltaic technology regarding the semiconductor cell, the solar panel design, and solar plant-operation.

Novel double-intrinsic layer heterojunction solar cells using a-Si/c-Si and CdS/CdSe were presented. These structures have a large photogeneration region with an in-built thermal management property due to the utilization of two materials with different energy gaps. More efficient material and structural compositions certainly exist, however the economic cost implications of solar cell production were also kept in mind. The proposed structures were only simulated, however, and should be manufactured and tested in order to verify or deny the achieved results.

A solar panel structure with a 20% mass reduction compared to the conventional configurations was suggested. Mainly, the replacement of the front glass surface with a hard-coated UV-resistant acrylic as well as the reconfiguration of the other encapsulating layers allowed us to achieve a lighter theoretical product. These reductions in a product's

mass could potentially translate to significant cost savings on shipping, installation, and handling. My optical, thermal, and wind load calculations and computer simulations showed a reasonable performance across all parameters. Several prototypes were manufactured to test the manufacturability of the design and the best approaches were suggested in the corresponding chapter.

Solar system installations are currently undergoing rapid growth and are introducing fundamental changes to the energy grid. Due to the inherent mismatch between the solar energy production peak and the consumer energy demand, in some states there is already an overproduction of solar energy occurring. This problem is likely to affect other states as well as the solar installation increase. The need in power production ramping flexibility as well as the measures of handling the power overproduction are becoming more and more apparent. Solar energy curtailment seems to be the most cost-efficient way of addressing this issue, and the use of solar curtailment as a temporary solution to this problem was advocated as a temporary solution. This work pointed out some problems in the currently implemented curtailment methods, proposed an alternative method, and outlined the implementation methods of the proposed approach. The guideline principles were described while leaving a possibility for them to be applied for a specific photovoltaic installation project due to the vast diversity of available technological approaches and regulatory circumstances.

APPENDIX A. MECHANICAL TRACKING SYSTEM DESIGN PROTOTYPE

I. Introduction

No new claims are made in this section. A design of a single-axis solar tracking is proposed in this chapter and its advantages and disadvantages are evaluated. Prior to that, the benefits of solar tracking over fixed-tilt systems, as well as mechanical aspects of conventional tracking systems are discussed. During the process of the prototype assembly, it was discovered that systems that use the same principle as the one proposed in this chapter already exist on the market. The assembly work was continued, however, to potentially run a threshold-tracking algorithm described in Chapter 6. The assembled prototype results of the proposed tracking system are provided at the end of the chapter.

A PV solar tracker is a device that keeps the angle of incidence of solar arrays on solar panels at an optimal minimum[9]. Two branches of solar tracking systems, differentiated by the number of degrees of freedom they have, are *single-axis* and *dual-axis* tracking systems (note: classification by other properties also exist. Example: active and passive, concentrating and non-concentrating, and others). Tracking systems increase the initial cost of the PV site as well as the Operation and Maintenance (O&M) costs, however PV solar

---

[9] Note: different from mechanically possible minimum. Mechanically possible minimum is not always desirable in tracking. A strategy called backtracking, for example, does not point the panels towards the sun in early mornings and late evenings but turns them slightly away to decrease shadowing and increased energy output. Another example being a strategy used in cloudy days that will be discussed later in this chapter.

tracking systems consistently outperform fixed-tilt mounting systems in the amount of energy harvested. The industry-recognized number for the average advantage of tracking systems over their fixed-tilt counterparts is 25-35% [97], [98], [99], and [100]. This number comes from the feasibility studies of solar PV sites done by the National Renewable Energy Laboratory (NREL). Due to this fact, more than half of utility-scale solar PV systems use solar tracking according to U.S. Energy Information Agency (EIA) [101]. A market research report by Global Market Insights predicts a 16% growth of solar tracker market by 2024, which is currently evaluated at more than USD 7 billion [102].

II. Angle-dependent Losses and Solar Motion

The main loss sources in PV systems are due to effective area and surface reflection under different insolation angles. The effective area defines the number of rays intercepted by the panel and is equal to the cosine of the angle between the incidence angle and normal to the panel's surface (refer to Figure 44). Losses due to reflection are insignificant until up to 50˚ and then they increase significantly to about 13% loss at 70˚and 60% at 80˚ (refer to figure 45). These incidence angle-dependent losses are only meaningful in the context of solar motion across the sky that introduces angular variations within a day and between seasons.
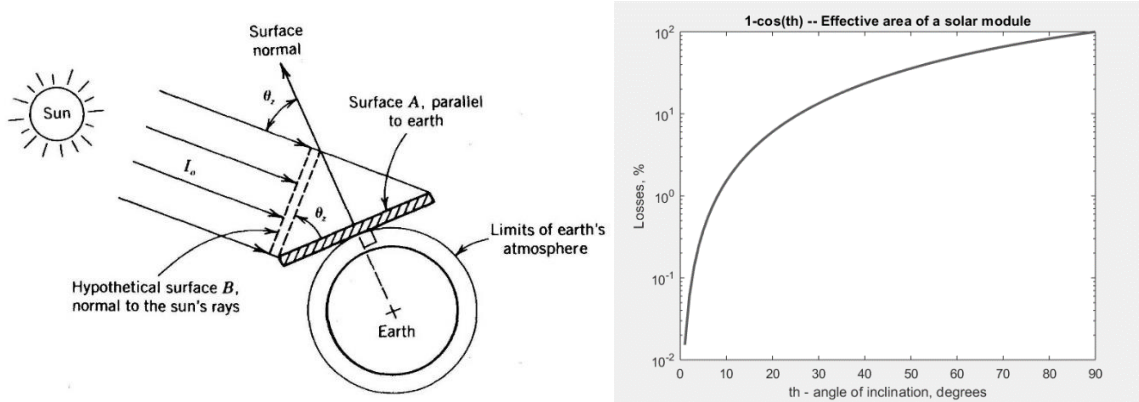
Figure 44 - Effective area loss due to insolation angle [103].   Figure 45 - Effective area calculation of a solar module.

Solar motion can be decoupled into elevation and azimuth components. It also has seasonal variations affecting both these components that are due to the Earth's axial tilt of 23.5° with respect to the plane of rotation around the sun. In order to understand these variations, it helps to consider only the March Equinox (around March 22nd), June Solstice (around June 22nd), September Equinox (around September 22nd), and December Solstice (around December 22nd), and extrapolate all other days as the in-between gradations of these special cases. Equinox is usually defined as the moment when the sun passes a celestial equator, but it is easier to understand when one refers to Figure 36. Note that the planetary tilt's projection on the plane of rotation at the equinoxes is adjacent to the orbit. In contrast, at the solstices, that projection is aligned with the orbit's radius. Equinoxes have special properties that make them perfect as points of reference: the length of the day is almost exactly 12 hours, the East-West motion of the sun is almost exactly 180°, the sun's zenith angle is equal to the altitude coordinate of the observer's location, and all these are true anywhere on the planet. The sun's elevation is 23.5° higher on June solstice (on the northern hemisphere) and 23.5° lower on December solstice. This implies that azimuthal motion is also more than 180° in Spring and Summer, but less in Fall and Winter. One can

refer to Tables 13 and 14 to better picture the solar motion span, Boston and San Diego were chosen to get a sense of site's geolocation on the sun's path.
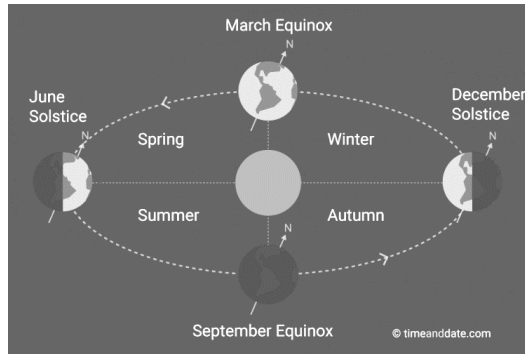
Figure 46 - Nature of geo motion. Image: [104]
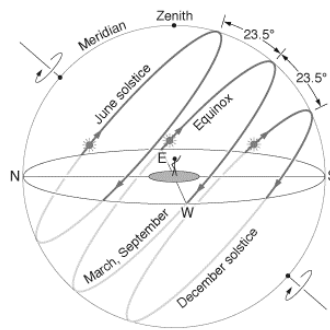
Figure 47 - Origin of seasons. Image: [105]

Table 13 - Boston, MA, Sun Path Sample Data.

Date	Time	Elevation	Azimuth	dAz
Spring Equinox 3/22/2019	Sunrise 6:50:00		89.1709	
	Midday 12:50:00	48.0873	179.1828	182
	Sunset 19:00:00		271.9311	
Summer Solstice 6/22/2019	Sunrise 5:10:00		56.7444	
	Midday 12:50:00	70.7997	181.8929	246
	Sunset 20:20:00		302.4781	
Fall Equinox 9/22/2019	Sunrise 6:40:00		90.0704	
	Midday 12:40:00	47.6244	180.7343	180
	Sunset 18:40:00		270.4568	
Winter Solstice 12/22/2019	Sunrise 8:10:00		121.4136	
	Midday 12:40:00	23.9644	179.0461	116
	Sunset 17:10:00		237.3080	

Table 14 - San Diego, CA, Sun Path Sample Data.

Date	Time	Zenith	Azimuth	dAz
Spring Equinox 3/22/2019	Sunrise 6:50:00		88.7766	
	Midday 13:00:00	57.7451	182.4070	183
	Sunset 19:00:00		271.4284	
Summer Solstice 6/22/2019	Sunrise 5:40:00		61.0676	
	Midday 12:50:00	80.434	180.0000	237
	Sunset 20:00:00		298.9200	
Fall Equinox 9/22/2019	Sunrise 6:40:00		89.6491	
	Midday 12:40:00	57.2031	179.6793	180
	Sunset 18:40:00		269.9980	
Winter Solstice 12/22/2019	Sunrise 7:50:00		118.0528	
	Midday 12:50:00	33.5826	180.9392	123
	Sunset 17:40:00		241.5175	

This gives the overall understanding of solar motion across the sky as well as the effect of seasonal variations of the solar path. Having this understanding, the advantages of dual-axis (2-A) tracking over single-axis (1-A) tracking systems can be evaluated. Smaller variations in the elevation angle throughout the day and throughout the seasons, and higher expenses associated with 2-A trackers, rarely make it cost-effective. According to the Energy Information Administration (EIA), only around 6% of the tracking systems used are dual-axis, whereas half of the remaining systems are single-axis trackers and the other half are fixed-tilt [101].

III. Single- vs. Dual-Axis Tracking

On average, dual-axis solar tracking provides a 35% increase in solar energy harvest compared to fixed-tilt systems, whereas single-axis system provides 25% [97], [98], [99], [100]. A literature search on this topic is tabulated in Table 16, where the comments and

references for each study are provided. Studies [106], [107], [108], [109], [110], [111], [112], and [113] allow one to appreciate the variations in possible power gains by tracking systems based on location and solar resource, and weather conditions. When singe-axis and dual-axis systems are compared within a single study, the average difference of 10% in favor of 2-A tracking is observed [111], [112], which corresponds to the NREL's assumptions. The most notable work was done in Greece [112] where more than 120 tracking devices in total were used. This study also noted a significant difference between the calculated and measured data and warns the plant design engineers as well as investors to consider this factor in their project evaluations.

Table 15 - Advantages of single- and dual-axis systems (1-A and 2-A tracking) over fixed-tilt counterparts.

Reference Number	%-Gain	Location	Comments
[106]	1-A: 20%	[Damascus, Syria]	Duration: a couple months of sunny summer days. 20% is the average daily gain. The study, however, provides the information about solar tracking performance during different hours within a day. According to the study, the tracking system introduces a gain of 40% during early morning and late evening hours and only 2-4% during mid-day.
[107]	1-A: 30-37%	Indore, India	Duration: one month. 10 sunny days, 17 sunny/normal cloudy and 4 heavily cloudy. 37% average gain during sunny days, 30% gain during sunny/cloudy conditions, 1.01% gain during cloudy conditions.
[108]	1-A: 12-20%	[Romania]	Duration: one month. Daily gain of 12-20% was observed and the variation is attributed to weather.
[109]	2-A: 23.4%	Southern Brazil	Duration: 152 days (40% of the days were cloudy/rainy). Average monthly gain ranged from 17.2%, in June, to 31.1%, in November.
[110]	2-A: 23.6%	Harbin, North-East China	Duration: several selected summer days
[111]	1-A: 28% 2-A: 40%	Cairo, Egypt	Duration: one year.
[112]	1-A: 25.2% 2-A: 34.5%	All prefectures of Greece	Measurements were collected by more than 40 single and 80 dual-axis PV plants. The study found high level of mismatch between calculated and measured data.
[113]	2-A: 25-45%	California, USA	Gain varies depending on the region with southwest and northeast being two poles of the gradient from high to low.

The feasibility of dual-axis solar tracking varies based on the geographical position of the site and thus the solar resources available in that region. Although dual-axis tracking adds 10% of efficiency on average to the overall energy harvest of the system, in many areas, those marginal gains might not be worth the risk and increased initial investment cost. A study by Lave and Kleiss provides a heatmap of dual-axis tracking's improvement over fixed-tilt systems for different regions (refer to Figure 48) [113].
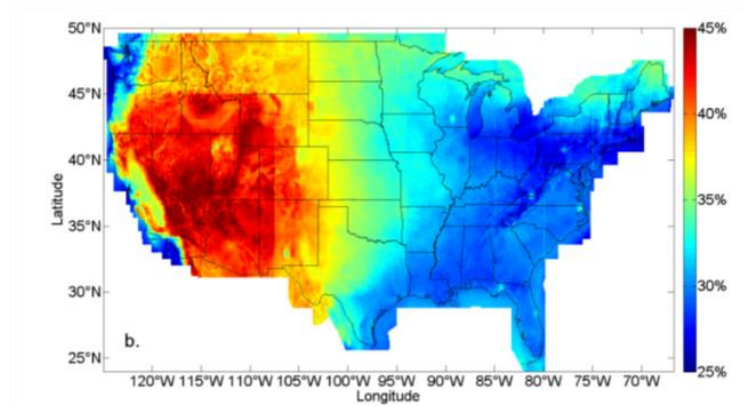
Figure 48 - Global Irradiance increase from fixed-tilt vs. Dual-Axis [113].

One can notice that the Northeastern region of America gets 25% increase and southwestern, 45%. However, the study done by US Energy Information Administration shows that even in these favorable conditions, dual-axis tracking is rarely deployed (refer to Figure 49) [101]. This means that the Return On Investment (ROI) of dual-axis tracking systems have to be carefully assessed and compared to single-axis tracking systems before deployment, especially in the eastern-northeastern region of the US.

Operable utility-scale solar photovoltaic generating units (2015)
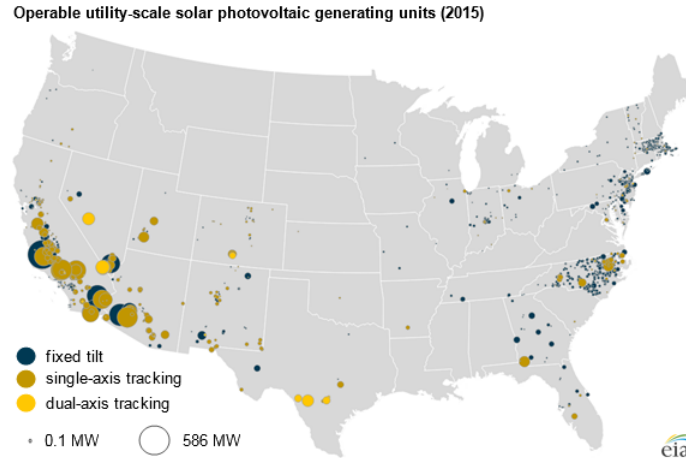
Figure 49 - Dual-Axis, Single-Axis, and Fixed Tilt systems distribution map [101].

IV. Existing Technology – Distributed and Aggregated Actuation Effort

Active solar tracking systems are electromechanical systems that maximize the harvest of a solar module by keeping a normal to its surface parallel to the solar irradiance angle throughout the day. There are many systems of classification of solar tracking systems, however this work will differentiate said systems as having either an aggregated or a distributed actuation effort. Aggregated actuation effort tracking systems have a single motor that simultaneously turns multiple strings of solar panels. In contrast, distributed actuation effort tracking systems have a motor either at each row or even at each individual mounting. This classification is justified because distributed and aggregated actuators have different operation and maintenance costs, complexities, and efficiencies. Large motors often costs less than many smaller motors that add up to the same power rating, and they have a lower maintenance cost. These claims will be supported in the following paragraphs.

Last year, TÜV Rheinland conducted an independent assessment of two solar sites with centralized and decentralized actuator architectures [114]. The study showed that aggregated layouts had a better lifetime cost-efficiency when the cost of possible

replacements as well as the overall number of points of failure were considered. This study, however, compared two single-axis tracking systems, one with a single 2 hp AC motor that controlled 32 rows (1 MW) and second architecture with a motor for each row. A market search showed no aggregated actuation effort dual-axis solar trackers, however the methodology and main principles established in TÜV Rheinland's study can be applied to evaluate such systems as well. The main design principle recommendations based on the study observations can be stated as follows:

- The number of electrical and mechanical components used should be reduced

- Components with long lifetimes should be used

- Torque tubes connected from a single motor to multiple rows, and bearings are maintenance free (This is speculated because the report did not include O&M expenses for these parts in their cost analysis. Since the sites that were examined were in use for about ten years each and no failures were reported, and since inter-row bearings and torque tubes don't carry the weights of the panels and operate within rated loads, this speculation is assumed to be reasonable).

Some of the existing dual-axis tracking and single-axis tracking systems are discussed in Table 15. The critical components used, tracker type and capacity, as well as some other information relevant to their long-term deployment is provided. This information is used as a reference for the proposed alternative system. It was later realized, however, that there is not enough difference between the proposed system, and the horizontal tilted single-axis tracker provided in Table 15.

Table 16. Existing solar tracking systems and their description.

	- **Product name:** DuraTrackAZ [115] - **Type:** vertical single axis - **Capacity:** 16 panels - **Motor:** 24 VDC, 36 W slew drive - 1MW power plant would require 175+ motors with a 10-year lifetime [116], [117]
	- **Product name:** DuraTrackHZ3 [118] - **Type:** horizontal single axis - **Capacity**: 90x32 panels - **Motor:** 2 HP, 3 PH, 480 VAC - 1MW power plant would require 1 motor and 64 vibration dampeners - This tracker was analyzed in TÜV Rheinland's study
	- **Product name:** ArcTracker [119] - **Type:** linked tilted single axis - **Capacity**: 20x11 modules - **Motor:** 150 W slew drive motor - 1MW would require 13 motors with a 10-year lifetime
	- **Product name:** PST-2AL Dual Axis Tracker [120] - **Type:** dual-axis (azimuth & vertical) - **Capacity**: 42-49 modules - **Motor:** 120 W DC slew drive, linear actuator 150 W DC. Lifetime of these specific motors is unknown, however similar motors on the market last 8-10 years. - 1MW station would require 60 slew drive and 60 linear motors - Weighs 1,970kg without panels
	- **Product name:** ST44M2V2P [121] - **Type:** dual-axis (tip-tilt) - **Capacity**: 2 modules - **Motors:** 2x48W linear actuators with 8-year lifetime - 1MW station would require 2800 linear actuators
	- **Product name:** Macsun Solar [122], ArcTracker [123] - **Type:** horizontal tilted single-axis - **Capacity:** 22, 24, or 60 - **Motors:** 2 slew-drive motors

V. Proposed System and Prototype Manufacturing

The proposed mechanical system is capable of tracking a change in solar motion in both elevation and azimuth with using only a single motor. Furthermore, several of such trackers can be connected in a row to be powered by a single larger motor to further decrease the cost of the system.
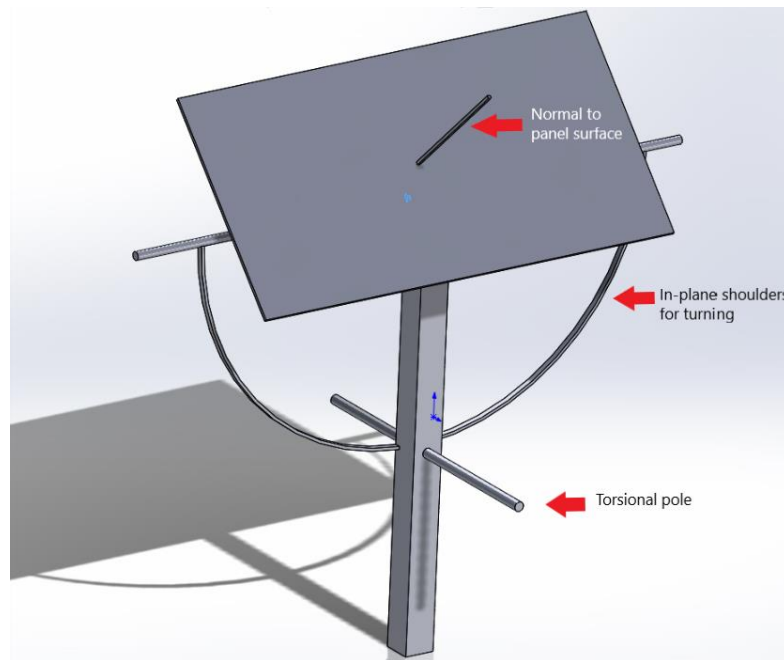
Figure 50 - Illustration of the proposed structure.

With a system configuration as shown in Figure 50, power is applied to the torsional pole either by a locally installed motor (autonomous operation) or by a large motor that turns several such structures in a row. The torsional pole moves the in-plane shoulder gear and the horizontal pole on which a solar module is resting tilts either to the left or to the right. Note that there is only one axis of rotation: the axis of rotation intersects the horizontal lever pole, is perpendicular to the vertical mounting pole, and is parallel to the torsional pole. If, however, one tracks the motion of the normal to the panel's surface, it moves in

two directions – both elevation and azimuth. Figures 51 (a-c) can help one picture this motion.
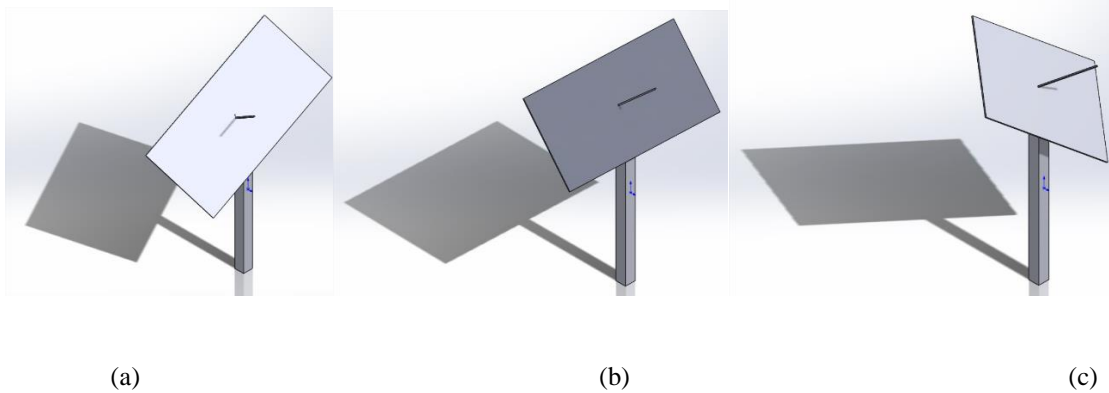
Figure 51 - Illustration of motion of the proposed mechanical system.

The big advantage of such a system is that in naturally follows the approximate path of the sun during the day and it does so using simple parts with few moving mechanisms. Thus, in terms of design requirements, it adheres to industry needs and has the potential to sufficiently decrease the cost of elevation-azimuth tracking to the level of simple single axis systems.

A prototype system was built in order to gain some insight into the manufacturability of the proposed system. During the process of assembling the prototype, it was found out that similar designs already exist on the market [122], [123]. The work was continued, however, with a hope of using this system in testing a threshold-tracking algorithm. Due to some design mistakes, however, the prototype did not work as expected. These mistakes and design improvement suggestions are provided later in the chapter. The detailed drawings are provided in Figures 52 and 53 (metal ropes, and solar panel attachments are not shown).
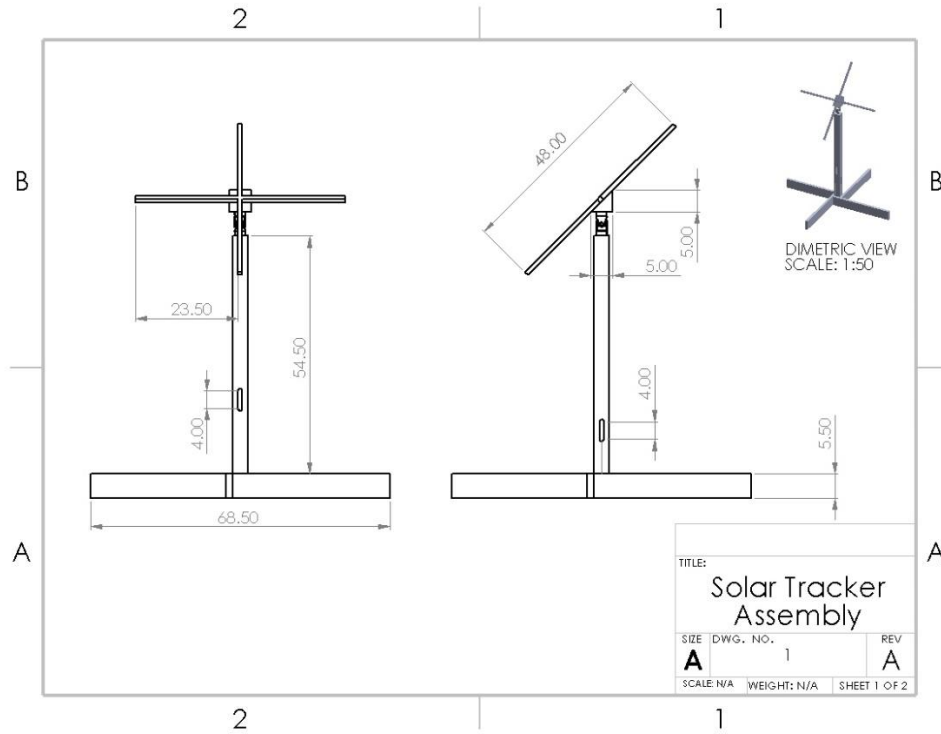
Figure 52 - Detailed drawing (Sheet 1)
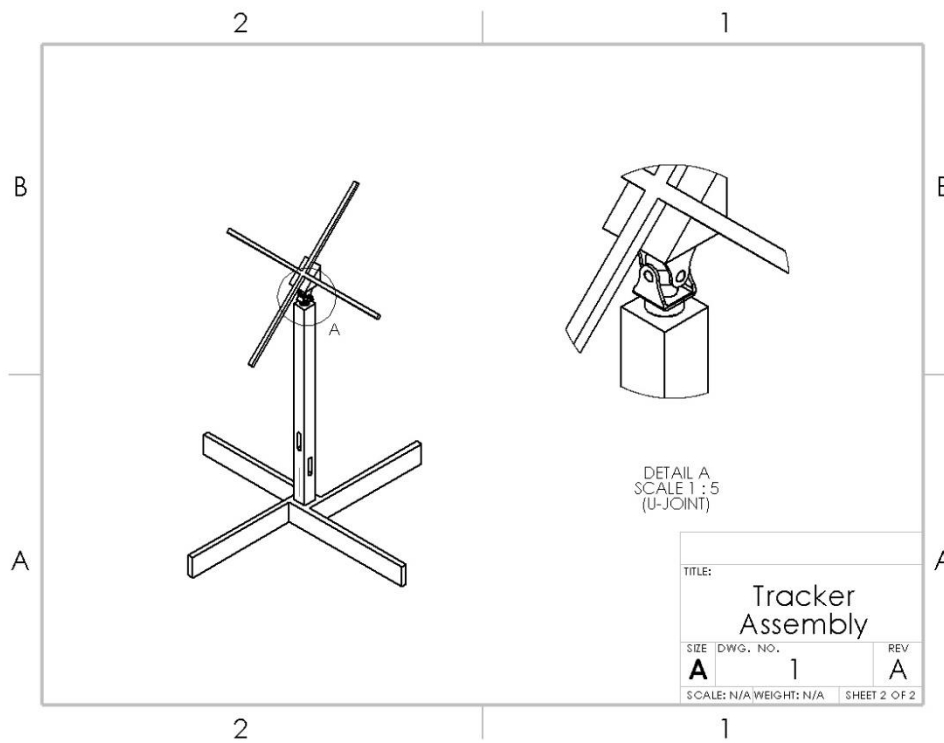
Figure 53 - Detailed drawing (Sheet 2)

The main pole was assembled, and a short torsional shaft was integrated into the pole as shown in Figures 54 and 55. In this stand-alone configuration, a motor that would actuate the rotation was directly mounted onto the main pole (refer to Figures 55 and 56). In larger-scale applications, however, the torsional shaft can be connected to multiple trackers in series and then to a single large motor.

Figure 54 - Main pole of the tracking system.

Figure 55 - Embedded torsional shaft.

Figure 56 - Motor mounting.

Figure 57 - 3D printed torque increasing sprocket pair connected with a rubber belt.

A 750 W DC motor was salvaged from an old treadmill, and a torque-increasing sprocket pair was custom designed and 3D printed. Figure 58 shows the lever arms of the tracker; note that the levers are connected to a U-joint. This is because, initially, a dual-axis design variation was approached but turned out to be impractical.

Figure 58 - Lever arms connected to a U-joint.

Figure 59 - Added dampers.

A couple of 33 lbs. dampers were used to shock absorb any sudden movement and to provide some time for the motor direction to safely reverse back and forth during threshold-tracking (refer to Figure 59). The fully assembled view of the prototype is provided in Figures 60 and 61. An elevation angle tracking lever pair was connected with a steel cable and pinned down to the main pole. The idea was to decouple the motion of the two axes. Ultimately, this was the main problem for the prototype's failure. It was mistakenly assumed that motion of a horizontal tracking axis will not affect the other axis, which is only true when the tilt angle is zero.

Figure 60 - Assembled prototype (front).   Figure 61 - Assembled prototype (back).
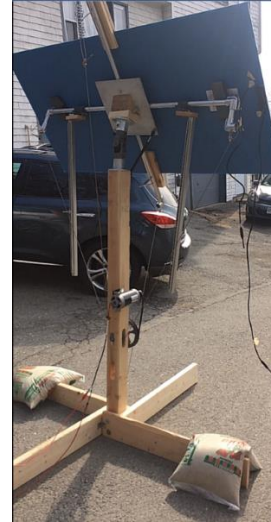
When the tilt angle is not zero, however, the plane of rotation of the vertical lever changes and if the two ends are tied to a metal cable with a constant length, the system starts to experience additional strains which deflect the entire structure. This problem is very easy to solve by replacing the u-joint with a regular one axis hinge.

Another mistake was made by leveraging the two shoulders of the tracker with a steel cable. When the horizontal levers turn, the length of the steel cable needs to decrease in order to maintain a good contact between the torsional shaft and the steel cable. This was later addressed by replacing a metal pulley and a metal rope with a large sprocket and a roller chain. This time the motor could turn a panel fully to one side, however when the direction of rotation is reversed, the motor could not apply enough torque to move the panel. This problem, however, could be solved by introducing a torque stepping-up gearbox because the motor has large rpms.

VI. Conclusion

This project started with an aim of proposing a novel mechanical solar tracking system that would be able to track the solar motion in both elevation and azimuth using only one motor. The design was also devised to be modular, allowing multiple such systems to be connected in a row and be driven by a single motor in order to increase the tracking operation efficiency. A preliminary market search did not show any similar products and so the design and manufacturing process started. Later, however, solar tracking systems operating on the same principles but slightly different in the mounting style were discovered [122], [123]. The work on the project continued with a hope to replicate the solar anti-tracking system and apply it to this tracker. However, that would have served no useful purpose because it would not have proven either that the anti-tracking is realizable in utility-scale solar applications or that any test results (even if successful) would translate to large scale PV systems. When the project faced a plethora of mechanical problems that are irrelevant to the course of study, the project was archived, and the results reported in the present appendix, instead of as one of the main chapters of this dissertation. The author gained plenty of valuable hands-on manufacturing experience, learned to effectively use CAD software, and gained insight into many Design-for-Manufacturing concepts and skills.

LITERATURE CITED

[1]   Bloomberg NEF, "New Energy Outlook 2018," Bloomberg, 2018.

[2]   NREL, "Advanced Inverter Functions to Support High Levels of Distributed Solar Policy and Regulatory Considerations," NREL, Golden, CO, 2014.

[3]   C. Jaquelin, M. Miller, O. Zinaman, M. Milligan, D. Arent, B. Palmintier, M. O'Malley, S. Mueller, E. Lannoye, A. Tuohy and et al., "Flexibility in 21st Century Power Systems," NREL, Golden, CO, 2014.

[4]   EIA, "What is U.S. electricity generation by energy source?," [Online]. Available: https://www.eia.gov/tools/faqs/faq.php?id=427&t=3. [Accessed 5 May 2019].

[5]   J. Hanschke, O. Dupre, M. Boccard and C. Ballif, "Silicon heterojunction solar cells: Recent technological development and practical aspects - from lab to industry," *Solar Energy Materials and Solar Cells,* vol. 187, pp. 140-153, 2018.

[6]   A. Marti and G. L. Araujo, "Limiting efficiencies for photovoltaic energy conversion in multigap systems," *Solar Energy Materials and Solar Cells,* vol. 43, no. 2, pp. 203-222, 1996.

[7]   T. P. White, N. N. Lal, K. R. Catchpole and et al., "Tandem Solar Cells Based on High-Efficiency c-Si Bottom Cells: Top Cell Requirements for >30% Efficiency," *IEEE Journal of Photovoltaics,* vol. 4, no. 1, pp. 208-214, 2013.

[8]   K. Yoshikawa, H. Kawasaki, W. Yoshida, T. Irie, K. Konishi and et al., "Silicon heterojunction solar cell with interdigitated back contacts for a photoconversion efficiency over 26%," *Nature Energy,* vol. 2, 2017.

[9]   D. D. Smith, P. Cousins, S. Westerberg and et al., "Toward the Practical Limits of Silicon Solar Cells," *IEEE Journal of Photovoltaics,* vol. 4, no. 6, pp. 1465-1469, 2014.

[10]   K. Masuko and et al., "Achievement of More Than 25% Conversion Efficiency With Crystalline Silicon Heterojunction Solar Cell," *IEEE Journal of Photovoltaics,* vol. 4, no. 6, pp. 1433-1435, 2014.

[11]   M. Tanaka and et al., "Development of New a-Si/c-Si Heterojunction Solar Cells: ACJ-HIT (Artificially Constructed Junction-Heterojunction with Intrinsic Thin-Layer)," *Japanese Journal of Applied Physics,* vol. 31, no. 11, 1992.

[12]   S. Mil'shtein and et al., "Optimization of Solar Energy Harvesting by Novel Solar Cells," in *International Conference on the Physics of Semiconductors*, Austin, TX, 2014.

[13]   L. Devarakonda, R. Kwende and S. Mil'shtein, "Design and Optical Analysis of Corrugated Surfaces for Silicon Solar Cell," *Scientific America,* 2012.

[14]   PVEducation, "Double Layer Anti Reflection Coatings," [Online]. Available: https://www.pveducation.org/pvcdrom/design-of-silicon-cells/double-layer-anti-reflection-coatings. [Accessed 5 May 2019].

[15]   S. De Wolf and et al., "High Efficiency Silicon Heterojunction Solar Cells: A Review," *Green,* vol. 2, no. 1, pp. 7-24, 2012.

[16]   S. De Wolf and et al., "Very fast light-induced degradation ofa-Si:H/c-Si(100) interfaces," *Physical review. B, Condensed matter,* vol. 83, no. 23, 2011.

[17]   Z. C. Holman and et al., "Current Losses at the Front of Silicon Heterojunction Solar Cells," *IEEE Journal of Photovoltaics,* vol. 2, no. 1, pp. 7-15, 2012.

[18]   R. Kwende, A. Pillai and S. Mil'shtein, "Hetero-structure p-i-n-i-p Solar Cell with Virtual Collector," *International Conference on Low Dimensional Structures & Devices,* p. 4, 2011.

[19]   Panasonic, "Panasonic HIT® Solar Cell Achieves World's Highest Conversion Efficiency of 24.7% at Research Level," 13 February 2013. [Online]. Available: https://news.panasonic.com/global/press/data/2013/02/en130212-7/en130212-7.html. [Accessed 5 May 2019].

[20]   A. Descoeudres and et al., ">21% Efficient Silicon Heterojunction Solar Cells on n- and p-Type Wafers Compared," *IEEE Journal of Photovoltaics,* vol. 3, no. 1, pp. 83-89, 2013.

[21]   W. G. v. Sark and et al., "Physics and Technology of Amorphous-Crystalline Heterostructure Silicon Solar Cells," *Engineering Materials,* vol. 0, pp. 1-12, 2012.

[22]   J. Mullerova and et al., "Microstructure Related Characterization Of a-Si:H Thin Films," *Advances in Electrical and Electronic Engineering,* vol. 6, no. 3, pp. 108-111, 2007.

[23]   A. G. Ulyashin and et al., "The influence of the amorphous silicon deposition temperature on the efficiency of the ITO/a-Si:H/c-Si heterojunction (HJ) solar cells and properties of interfaces," *Thin Solid Films,* Vols. 403-404, pp. 359-362, 2002.

[24]   S. Mil'shtein and M. Zinaddinov, "Cascaded Heterostructured a-Si/c-Si Solar Cell with Increased Current Production," in *Proceedings IEEE 43rd International Conference of Photovoltaic Specialists*, 2016.

[25]   Fraunhofer Institute for Solar Energy Systems, "Photovoltaics Report," 2016.

[26]   H. Park and et al., "Enhancement of Photo-Current Conversion Efficiency in a CdS/CdSe Quantum-Dot-Sensitized Solar Cell Incorporated with Single-Walled Carbon Nanotubes," *J Nanosci Nanotechnol,* vol. 15, no. 2, 2015.

[27]   X. Mathew and et al., "CdTe/CdS solar cells on flexible substrates," *Solar Energy,* vol. 77, no. 6, pp. 831-838, 2004.

[28]   NREL, "Cadmium Telluride Solar Cells," [Online]. Available: https://www.nrel.gov/pv/cadmium-telluride-solar-cells.html. [Accessed 5 May 2019].

[29]   W.-D. Park, "Nanocrystalline CdS thin films prepared by chemical bath deposition," in *Nanotechnology Materials and Devices Conference*, 2006.

[30]   S. Sze, Physics of Semiconductor Materials, John Wiley & Sons, 1985.

[31]   J. Wysoki, "Effect of temperature on Photovoltaic Solar Energy conversion," *Jour. of App. Physics,* vol. 31, no. 3, 1960.

[32]   S. Mil'shtein, M. Zinaddinov and et al., "Design and Fabrication Steps of Silicon Heterostructured p-i-i-n Solar Cell with Corrugated Surface," in *IEEE PVSC Proceedings*, Portland, 2016.

[33]   S. Mil'shtein, A. Pillai, S. Sharma and G. Yessayan, "Design of Cascaded Low Cost Solar Cell with CuO Substrate," *Intern. Confer. Phys. Semicond.,* 2012.

[34]   S. K. Tripathy and et al., "Mobility lifetime product in doped and undoped nanocrystalline CdSe," *Thin Solid Films,* vol. 548, pp. 406-410, 2013.

[35]   Sigma-Aldrich, "Silicon," [Online]. Available: http://www.lesker.com/newweb/deposition_materials/depositionmaterials_sputtertargets_1.cfm?pgid=si1. [Accessed 5 June 2017].

[36]   Sigma-Aldrich, "Cadmium selenide," [Online]. Available: https://www.sigmaaldrich.com/catalog/product/aldrich/217921?lang=en&region=US&cm_sp=Insite-_-recent_fixed-_-recent5-2. [Accessed 5 June 2017].

[37]   Sigma-Aldrich, "Cadmium sulfide," [Online]. Available: https://www.sigmaaldrich.com/catalog/product/aldrich/217921?lang=en&region=US&cm_sp=Insite-_-recent_fixed-_-recent5-2. [Accessed 5 May 2019].

[38]   Kurt J. Lesker Company, "Cadmium Sulfide (CdS) Sputtering Targets," [Online]. Available: https://www.lesker.com/newweb/deposition_materials/depositionmaterials_sputtertargets_1.cfm?pgid=cd3. [Accessed 5 May 2019].

[39]   Kurt J. Lesker, "Silicon (Si) Sputtering Targets," [Online]. Available: https://www.lesker.com/newweb/deposition_materials/depositionmaterials_sputtertargets_1.cfm?pgid=si1. [Accessed 5 May 2019].

[40]   A. M. Barnett and et al., "Thin-film solar cells: Aunified analysis of their potential," *Electron Devices,* vol. 27, no. 4, pp. 615-630, 1980.

[41]   H. Ullal, "National Solar Technology Roadmap: CdTe PV," Energy Efficiency and Renewable Energy, 2007.

[42]   R. Fu and et al., "U.S. Solar Photovoltaic System Cost Benchmark: Q1 2018," NREL, 2018.

[43]   US Environmental Protection Agency, "Solar Photovoltaic. Specification, Checklist and Guide," 2011.

[44]   G. Sampson, "Solar Power Installations on Closed Landfills: Technical and Regulatory Considerations," 2009.

[45]   B. Marion and et al., "Performance Parameters for Grid-Connected PV Systems," in *The 31st IEEE Photovoltaics Specialists Conference and Exhibition*, Lake Buena Vista, Florida, 2005.

[46]   F. A. Mejia and et al., "Soiling losses for solar photovoltaic systems in California," *Solar Energy,* vol. 95, 2013.

[47]   C. Thurston, "Ensuring Your Solar Array Doesn't Get Caught in the Wind," Renewable Energy World, 20 July 2015. [Online]. Available: https://www.renewableenergyworld.com/articles/print/volume-18/issue-4/features/solar/ensuring-your-solar-array-doesn-t-get-caught-in-the-wind.html. [Accessed 8 May 2019].

[48]   Ecoprogetti, "The Structure of a Photovoltaic Module," [Online]. Available: https://ecoprogetti.com/the-structure-of-photovoltaic-module/. [Accessed 5 May 2019].

[49]   P. DiSessa, "What Goes Into Making A Solar Module?," [Online]. Available: https://www.solarpowerworldonline.com/2013/04/what-goes-into-making-a-solar-module/. [Accessed 5 May 2019].

[50]   O. Kretschmann, "Curable polyorganosiloxane composition for use as an encapsulant for a solar cell module". USA Patent 9,543,460, 7 March 2013.

[51]   B. E. Bunea and et al., "Photovoltaic module and laminate". Patent 9,914,286, 3 1 2013.

[52]   L. Jun and et al., "Polymer interlayers having improved optical properties". Worldwide Patent WO2014/200989A3, 8 June 2017.

[53]   GES, "Solar PV Modules," 2016.

[54]   AcmePlastic, "Acrylic Cast Clear Sheet," [Online]. Available: https://www.acmeplastics.com/acrylic-sheets/acrylic-cast-clear-sheet. [Accessed 5 May 2019].

[55]   Glasscages.com, "Custom Size Cut Sheets of Glass," [Online]. Available: http://www.glasscages.com/?sAction=ViewCat&lCatID=42. [Accessed 5 May 2019].

[56]   Abrisa Technologies, "Specialty Glass ProductsTechnical Reference Document," 5 May 2019. [Online]. Available: chrome-

extension://oemmndcbldboiebfnladdacbdfmadadm/http://abrisatechnologies.com/specs/Soda-Lime%20Low%20Iron%20Spec%20Sheet%20072012.pdf. [Accessed 5 May 2019].

[57] Arkema, "Plexiglass," [Online]. Available: https://www.plexiglas.com/export/sites/plexiglas/.content/medias/downloads/sheet-docs/plexiglas-guf3-guf4.pdf. [Accessed 5 May 2019].

[58] EnergySage, "Types of Solar Panels," 26 February 2019. [Online]. Available: https://www.energysage.com/solar/101/types-solar-panels/. [Accessed 5 May 2019].

[59] GreenMatch, "7 Different Types of Solar Panels Explained," 1 April 2019. [Online]. Available: https://www.greenmatch.co.uk/blog/2015/09/types-of-solar-panels. [Accessed 5 May 2019].

[60] Energy Informative, "Which Solar Panel Type is Best? Mono- vs. Polycrystalline vs. Thin Film," [Online]. Available: https://energyinformative.org/best-solar-panel-monocrystalline-polycrystalline-thin-film/. [Accessed 5 May 2019].

[61] EnergySage, "New solar panels: what's coming to market in 2019?," [Online]. Available: https://news.energysage.com/new-solar-panels-whats-coming-market-2018/. [Accessed 5 May 2019].

[62] Dow Corning, "Sylgard® 184Silicone Elastomer," [Online]. Available: https://web.mit.edu/sriram/Public/Graphics/Sylgard184Datasheet.pdf. [Accessed 5 May 2019].

[63] MIT, "Material Property Database," [Online]. Available: https://web.mit.edu/6.777/www/matprops/pdms.htm. [Accessed 5 May 2019].

[64] Sandia, "Sylgard 184: Young's modulus at 23C," 2010. [Online]. Available: https://www.sandia.gov/polymer-properties/E1-Youngs_modulus.html. [Accessed 5 May 2019].

[65] I. D. Johnston, "Mechanical characterization of bulk Sylgard 184 for microfluidics and microengineering," *J. Micromech. Microeng,* vol. 24, 2014.

[66] Celanese, "COOLPOLY D3612 Properties," [Online]. Available: http://tools.celanese.com/. [Accessed 5 May 2019].

[67] P. Plastics, "Mechanical Properties of Plastic Materials," [Online]. Available: https://www.professionalplastics.com/professionalplastics/MechanicalPropertiesofPlastics.pdf. [Accessed 5 May 2019].

[68] RefractiveIndex.info, "Optical constants of BK7," [Online]. Available: https://refractiveindex.info/?shelf=glass&book=BK7&page=SCHOTT). [Accessed 5 May 2019].

[69] K. R. McIntosh and et al., "An optical comparison of silicone and EVA encapsulants for conventional silicon PV modules: A ray-tracing study," in *Proceeding of the 34th IEEE Photovoltaic Specialists Conference*, Philadelphia, 2009.

[70] L. Gao and et al., "Refractive index determination of SiO2 layer in the UV/Vis/NIR range: spectrophotometric reverse engineering on single and bi-layer designs," *J. Europ. Opt. Soc. Rap. Public.,* vol. 8, 2013.

[71] K. R. McIntosh and et al., "Increase in external quantum efficiency of encapsulated silicon solar cells from a luminescent down-shifting layer," *Progress in Photovoltaics: Research and Applications,* pp. 191-197, 2009.

[72] L. M. Moore and et al., "Five Years of Operating Experience at a Large, Utility-scale Photovoltaic Generating Plant," *Progress in Photovoltaics: Research and Applications,* 2008.

[73] J. Sterling and et al., "Proactive Solutions To Curtailment Risk. Identifying New Contract Structures For Utility-Scale Renewables," SEPA & ScottMadden, 2016.

[74] B. Kropolski and et al., "Achieving a 100% Renewable Grid," *IEEE Power & Energy Magazine,* vol. 15, no. 2, pp. 61-73, 2017.

[75] Center for Sustainable Systems, UMich, "U.S. Grid Energy Storage Factsheet," 2017.

[76] Solar Energy Industries Assosiation, "Solar Industry Research Data," 2019.

[77] ScottMadden, "Solar Photovoltaic Plant Operating and Maintenance Costs," 2010.

[78] Bloomberg NEF, "Clean Energy Investment Exceeded $300 Billion Once Again in 2018," 16 January 2018. [Online]. Available: https://www.eia.gov/tools/faqs/faq.php?id=427&t=3. [Accessed 5 May 2019].

[79] Imperial College London (via EdX), "Incorporating Renewable Energy in Electricity Grids," [Online]. Available: courses.edx.org/courses/course-v1:ImperialX+dacc003+3T2018/courseware/1adef2ea5bfe4305a6985e14311f28a6/834a5237a9784c528a3be61b0f1d37d2/2?activate_block_id=block-v1%3AImperialX%2Bdacc003%2B3T2018%2Btype%40vertical%2Bblock%40aa42bc09f7404d46930f036ed6cc1dd. [Accessed 2 February 2019].

[80] CAISO, "What the duck curve tells us about managing a green grid," 2016. [Online]. Available: http://www.caiso.com/Documents/FlexibleResourcesHelpRenewables_FastFacts.pdf. [Accessed 5 May 2019].

[81] CAISO, "Impacts of renewable energy on grid operations," 2017. [Online]. Available: Impacts of renewable energy on grid operations. [Accessed 5 May 2019].

[82] California ISO, "Managing Oversupply," [Online]. Available: http://caiso.com/informed/Pages/ManagingOversupply.aspx. [Accessed 5 May 2019].

[83]   CAISO, "Monthly Renewables Performance Report," 2019. [Online]. Available: http://www.caiso.com/Documents/MonthlyRenewablesPerformanceReport-Mar2018.html. [Accessed 5 May 2019].

[84]   Hawaiian Electric Companies, "PSIPs Update Report," 2016.

[85]   TI, "HighVoltageSolarInverterDC-ACKit," 2014.

[86]   A. Bindra, "Synchronous Rectification Gives Step-Up Converters a Boost," 2014.

[87]   M. He, "Synchronous or Nonsynchronous Topology? Boost System Performance with the Right DC-DC Converter," Maxim Integrated, [Online]. Available: https://www.maximintegrated.com/en/app-notes/index.mvp/id/6129. [Accessed 5 May 2019].

[88]   ROHM Semiconductor, "Calculation of Power Loss (Synchronous)," November 2016. [Online]. Available: http://rohmfs.rohm.com/en/products/databook/applinote/ic/power/switching_regulator/power_loss_appli-e.pdf. [Accessed 5 May 2019].

[89]   VISHAY Siliconix, "Zero-Voltage Switching Full-Bridge Converter: Operation, FOM, and Guidelines for MOSFET Selection," 15 December 2014. [Online]. Available: Zero-Voltage Switching Full-Bridge Converter: Operation, FOM, and Guidelines for MOSFET Selection. [Accessed 5 5 2019].

[90]   S. Oliver, "Hard Facts on Soft Switching," Electronic Design, 30 September 2013. [Online]. Available: https://www.electronicdesign.com/power/hard-facts-soft-switching. [Accessed 5 May 2019].

[91]   S. Soman and e. al., "A Literature Review on Soft Switching DC-AC Converters," *IJERT,* vol. 3, no. 7, 2014.

[92]   SMA, "Device for Power Control of PV Plants. Power Reducer Box. User's Manual".

[93]   NY Solar Smart DG Hun, "Smart Grid Communications," DGHub, 2016.

[94]   E. Reiter, "Industry Perspectives on Advanced Inverters for U.S. Solar Photovoltaic Systems: Grid Benefits, Deployment Challenges, and Emerging Solutions," September 2015. [Online]. Available: https://www.nrel.gov/docs/fy15osti/65063.pdf. [Accessed 5 May 2019].

[95]   Satcon Inverter Solutions, "Modbus TCP/IP and RS485 Communications," 2011. [Online]. Available: https://deckmonitoring.zendesk.com/hc/en-us/article_attachments/209391028/PM00488-R3.pdf. [Accessed 5 5 2019].

[96]   K. Soga, "Influences of Solar Incident Angle on Power Generation Efficiency of PV Modules under Field Conditions," *Journal of Asian Architecture and Building Engineering,* vol. 2, no. 2, pp. 43-48, 2003.

[97]   B. Stoltenberg and e. al., "Feasibility Study of Economics and Performance of Solar Photovoltaics at the Former Fort Ord Army Base Site in Marina, California," NREL, 2013.

[98]   J. Simon and e. al., "Feasibility Study of Economics and Performance of Solar Photovoltaics at the Kerr McGee Site in Columbus, Mississippi," NREL, 2013.

[99]   J. Salasovich and e. al., "Feasibility Study of Economics and Performance of Solar Photovoltaics at the TechCity East Campus Resource Conservation and Recovery Act Site in Kingston, New York," NREL, 2014.

[100]   S. J. and e. al., "Feasibility Study of Economics and Performance of Solar Photovoltaics at the Price Landfill Site in Pleasantville, New Jersey," NREL, 2013.

[101]   S. Hoff and e. al., "More than half of utility-scale solar photovoltaic systems track the sun through the day," EIA, 2017.

[102]   A. Gupta and e. al., "Solar Tracker Market Size By Technology (CSP, PV, CPV (LC,HC)), By Product (Single-Axis (Horizontal, Vertical), Dual-Axis), By Application, Industry Analysis Report, Regional Outlook, Price Trends, Competitive Market Share and Frecast, 2017-2024," GM Insights, 2017.

[103]   W. Stine and M. Geyer, "Power from the Sun"," [Online]. Available: http://www.powerfromthesun.net/Book/chapter02/chapter02.html. [Accessed 5 May 2019].

[104]   timeanddate.com, "The September Equinox," [Online]. Available: https://www.timeanddate.com/calendar/september-equinox.html. [Accessed 5 May 2019].

[105]   D. V. Schroeder, "The Sun and the Seasons," 2011. [Online]. Available: https://physics.weber.edu/schroeder/ua/sunandseasons.html. [Accessed 5 May 2019].

[106]   A. Al-Mohamad and e. al., "Efficiency improvements of photo-voltaic panels using a Sun-tracking system," *Applied Energy,* vol. 79, no. 3, pp. 345-354, 2004.

[107]   S. P. Singh and e. al., "Performance Comparison and Cost Analysis of Single Axis Tracking and Fixed Tilt PV Systems," *Proc. of Int. Conf. on Current Trends in Eng., Science and Technology, ICCTEST,* 2017.

[108]   G. C. Lazaroiu and e. al., "Comparative analysis of fixed and sun tracking low power PV systems considering energy consumption," *Energy Conversion and Management,* vol. 92, pp. 143-148, 2015.

[109]   F. M. Hoffman and e. al., "Monthly profile analysis based on a two-axis solar tracker proposal for photovoltaic panels," *Renewable Energy,* vol. 115, pp. 750-759, 2018.

[110]   Y. Yao and e. al., "A multipurpose dual-axis solar tracker with two tracking strategies," *Renewable Energy,* vol. 72, no. 88-98, 2014.

[111] M. S. Elsherbiny and e. al., "Design Of Single-Axis And Dual-Axis Solar Tracking Systems Protected Against High Wind Speeds," *International Journal Of Scientific & Technology Research,* vol. 6, no. 9, pp. 84-89, 2017.

[112] A. G. Vokas and e. al., "Single and Dual Axis PV Energy Production Over Greece: Comparison Between Measured and Predicted Data," *Energy Procedia,* vol. 74, pp. 1490-1498, 2015.

[113] M. Lave and e. al., "Optimum fixed orientations and benefits of tracking for capturing solar radiation in the continental United States," *Renewable Energy,* vol. 36, no. 3, pp. 1145-1152, 2011.

[114] TÜV Rheinland PTL, LLC, "Risk and Economic Analysis on Two Tracker Architectures," TÜV Rheinland PTL, Tempe, Arizona, 2017.

[115] Array Technologies, "DuraTrackAZ SolarTracker," [Online]. Available: https://www.solaris-shop.com/content/DuraTrack%20AZ%20Specifications.pdf. [Accessed 5 May 2019].

[116] SAT Controls, "Slewing drive SD5 M3, table w. ball bearing 7400 / SD5M3," SAT Control, [Online]. Available: http://www.solar-motors.com/gb/slewing-drive-sd5-m3-table-w-ball-bearing-7400-sd5m3-i559.shtml?tselimage=3539#images. [Accessed 5 May 2019].

[117] SAT Controls, "9 inch SE9 solar tracker slewing drive with 24V DC motor from China manufacturer – XZWD," SAT Controls, [Online]. Available: https://www.alibaba.com/product-detail/9-inch-SE9-solar-tracker-slewing_60810380013.html?s=p. [Accessed 5 May 2019].

[118] ArrayTechnologies, "DuraTrack HZ v3," ArrayTechnologies, [Online]. Available: http://www.arraytechinc.com/wp-content/uploads/2018/09/array-technologies-duratrack-hz-v3-datasheet-1.pdf. [Accessed 5 May 2019].

[119] Arctech Solar, "Tilt Single Axis Tracker," Arctech Solar, [Online]. Available: http://www.arctrackerinc.com/wp-content/uploads/Tilt-Single-Axis-Tracker-Spec.pdf. [Accessed 5 May 2019].

[120] SunAction Trackers, "PST-2AL Dual Axis Tracker," SunAction Trackers, [Online]. Available: http://www.sat-energy.com/wp-content/uploads/2016/04/PST-2AL-Dual-Axis-Tracker.pdf. [Accessed 5 May 2019].

[121] SAT Control, "Solar Tracker 2-axis ST44M2V2P w backstr. for 2 pan. / 0124 / ST44M2V2P, without main pole and ground screws," SAT Control, [Online]. Available: http://www.solar-motors.com/gb/solar-tracker-2-axis-st44m2v2p-w-backstr-for-2-pan-0124-st44m2v2p-without-main-pole-and-ground-screws-i202.shtml. [Accessed 5 May 2019].

[122] Macsun Solar, "Horizontal Tilted Single Axis PV Tracker," Macsun Solar, [Online]. Available: http://www.macsunsolar.com/en/showpro.php?id=142. [Accessed 5 May 2019].

[123] ARC Tracker, "Horizontal Single Axis Tracker with Tilt Module," ARC Tracker, [Online]. Available: http://www.arctrackerinc.com/horizontal-single-axis-tracker-tilt-module/. [Accessed 5 May 2019].

[124] EnergySage, "How hot do solar panels get? Effect of temperature on solar performance," 1 January 2019. [Online]. Available: https://news.energysage.com/solar-panel-temperature-overheating/. [Accessed 5 May 2019].

[125] A. Faizan, "Solar Panel Data Sheet: Specification & Parameters," [Online]. Available: http://electricalacademia.com/renewable-energy/solar-panel-data-sheet-specification-parameters/. [Accessed 5 May 2019].

[126] M. Zinaddinov, S. Mil'shtein and et al., "Design of Cascaded Heterostructured p-i-i-n CdS/CdSe Low Cost Solar Cell," *Proceed. IEEE 44rd Intern. Confer. on Photovolt. Specialists,* 2017.